

Tracer diffusion under a concentration gradient: A pathway for a consistent development of mobility databases in multicomponent alloys



Daniel Gaertner^a, Julia Kundin^b, Neelamegan Esakkiraja^{a,d,*}, Jasper Berndt^e,
Adeline Durand^c, Josua Kottke^a, Stephan Klemme^e, Guillaume Laplanche^c,
Gunther Eggeler^c, Gerhard Wilde^a, Alope Paul^d, Ingo Steinbach^b, Sergiy V. Divinski^a

^a Institute of Materials Physics, University of Münster, 48149 Münster, Germany

^b ICAMS, Ruhr-Universität Bochum, 44801 Bochum, Germany

^c Institut für Werkstoffe, Ruhr-Universität Bochum, 44801 Bochum, Germany

^d Department of Materials Engineering, Indian Institute of Science, Bangalore 560012, India

^e Institute of Mineralogie, University of Münster, 48149 Münster, Germany

ARTICLE INFO

Article history:

Received 8 June 2022

Received in revised form 9 September 2022

Accepted 20 September 2022

Available online 3 October 2022

Keywords:

Tracer diffusion

Interdiffusion

Pair-wise diffusion model

ABSTRACT

Diffusion in the CoCrFeMnNi high-entropy alloy is investigated using an augmented tracer / interdiffusion couple approach. The tracer diffusion coefficients are measured along the diffusion path developed between the $\text{Co}_{17}\text{Cr}_{20}\text{Fe}_{20}\text{Mn}_{20}\text{Ni}_{23}$ and $\text{Co}_{23}\text{Cr}_{20}\text{Fe}_{20}\text{Mn}_{20}\text{Ni}_{17}$ end-members allowing an elaboration of a consistent composition-dependent diffusion database. Both tracer and chemical concentration profiles are successfully reproduced to a tolerable level using a pair-diffusion model avoiding the reference element concept. Up-hill diffusion of Co in the experimental profile is not reproduced by the existing kinetic and thermodynamic databases. The reasons for this mismatch are discussed. The calculation of intrinsic and interdiffusion coefficients from the estimated tracer diffusion coefficients utilizing the thermodynamic parameters is demonstrated. The calculated values of the interdiffusion coefficients produced a reasonable match with the interdiffusion flux profiles developed in the multicomponent diffusion couple. The calculation of the vacancy wind effect indicates its strong influence on several intrinsic cross diffusion coefficients.

© 2022 Elsevier B.V. All rights reserved.

1. Introduction

Diffusion phenomena in high-entropy alloys (HEAs) are in the focus of intensive research nowadays [1–4]. Especially, the so-called Cantor alloy [5], i.e. equiatomic CoCrFeMnNi, serves as a model system for both experimental and theoretical studies [6–9]. Inter-[10,11] and tracer-diffusion measurements were performed in both, polycrystalline [12,13] and single-crystalline [14,15] CoCrFeMnNi HEAs and a certain retardation of the diffusion rates with respect to diffusion in pure Ni and binary/ternary alloys was reported, analyzing the Arrhenius-type dependencies established for a temperature interval of 1100–1373 K [10,12–14]. Very recently, strong deviations from the otherwise linear temperature dependencies were found for Co and Ni diffusion in CoCrFeMnNi below about

1000 K [15]. These features were interpreted as hints towards potential short-range ordering in this alloy.

For technological applications and predictive capabilities to forecast the long-term stability of the materials, an assessment of the mobility parameters in broad composition/temperature intervals are required. Thus, in order to develop a consistent database with extended capabilities of diffusion modeling in the entire CoCrFeMnNi system, tremendous efforts would be required to measure tracer diffusion coefficients of all elements on a huge number of homogeneous alloys of different compositions. The approach developed by Belova and Murch [16,17] based on the seminal work by Manning [18] represents a break-through, allowing the determination of tracer diffusion coefficients as a function of composition along the diffusion path developed between two selected alloys. Furthermore, a contribution of grain boundary diffusion could easily be distinguished using the tracer technique, that allows the determination of true volume self diffusion contributions.

In our previous study [19], an augmented tracer-interdiffusion couple approach has been elaborated further and the concentration-dependent tracer diffusion coefficients and the tracer diffusion

* Corresponding author at: Institute of Materials Physics, University of Münster, 48149 Münster, Germany.

E-mail address: eneelame@uni-muenster.de (N. Esakkiraja).

coefficients of the unaffected end-members of the diffusion couple between $\text{Co}_{15}\text{Cr}_{20}\text{Fe}_{20}\text{Mn}_{20}\text{Ni}_{25}$ and $\text{Co}_{25}\text{Cr}_{20}\text{Fe}_{20}\text{Mn}_{20}\text{Ni}_{15}$ were determined. (We will use the abbreviation Co-15/25 for this couple throughout this paper). The concentration dependent tracer diffusion coefficient of Co was found to follow a non-monotonous behavior, which was influenced by contaminant up-hill diffusion of Mn, whereas the end-member diffusion coefficients of Co, Fe and Mn were in a good agreement with the determined trends for the intermediate concentrations. Based on these experimentally determined atomic mobilities, the prediction of the CALPHAD-type diffusion simulations using a new ansatz for the generalized diffusion model was found to be more exact than using other existing kinetic databases with Fe or Ni as the reference elements [20,21].

The present work is focused on combined radiotracer and interdiffusion experiments in a diffusion couple between $\text{Co}_{17}\text{Cr}_{20}\text{Fe}_{20}\text{Mn}_{20}\text{Ni}_{23}$ and $\text{Co}_{23}\text{Cr}_{20}\text{Fe}_{20}\text{Mn}_{20}\text{Ni}_{17}$ HEAs using the augmented tracer-interdiffusion couple approach [19] (hereafter this couple will be designated as Co-17/23). The analysis demonstrated in this study explains the possibility to determine all necessary diffusion parameters, namely the concentration-dependent tracer, intrinsic and the interdiffusion coefficients utilizing the relations proposed by Darken-Manning [22,23]. In the process, this analysis highlights the role of the vacancy wind effect in multicomponent diffusion. The measurements are combined with CALPHAD-type modeling of interdiffusion using a pair-diffusion approach [24]. Such tracer diffusion estimation under the boundary condition of a concentration gradient will be shown to provide a pathway for a consistent development of mobility databases for multicomponent alloys.

2. Methodology

2.1. Experimental methods

Pure elements (purity > 99.9 wt%) were purchased from the company HMV Hauner Metallische Werkstoffe. As the surfaces of the as-received Co and Mn flakes were oxidized, these two raw metals were etched in aqueous solutions of hydrochloric acid (18.5 vol. HCl) and nitric acid (> 5 vol% HNO_3), respectively. For more details about our etching procedures of Mn and Co, the reader may refer to Refs. [25,26], respectively. Moreover, as Mn has a low vapor pressure, 0.2 wt% extra Mn (normalized with respect to the total ingot's weight) was added to compensate for its loss during melting. All the raw elements were then inserted into a vacuum arc-melter of type AM 200 (Bühler AG), the chamber was purged with Ar twice before being filled up a third time with Ar to a partial pressure of 700 mbar. Residual amounts of oxygen were further reduced by melting about 40 g Ti in the chamber. Buttons of 64 g each were remelted five times and flipped upside down between each remelting step to ensure a good chemical homogeneity. During the last remelting step, the melt was drop-cast into a cylindrical copper mold with a diameter of 6 mm and a height of 71 mm. The solidified alloys were then encapsulated in evacuated quartz tubes (3×10^{-5} mbar) and homogenized in a furnace at 1473 K for 2 days. Finally, the homogenized rods were sliced perpendicularly to their longitudinal axes into 1 mm thick disks that were used as end-members of the diffusion couples.

The alloy compositions were measured using an Electron Probe Microanalyser (EPMA) JEOL-JXA-8530F and determined as $\text{Co}_{16.9}\text{Cr}_{20.5}\text{Fe}_{20.0}\text{Mn}_{20.2}\text{Ni}_{22.4}$ and $\text{Co}_{22.6}\text{Cr}_{20.6}\text{Fe}_{20.1}\text{Mn}_{20.2}\text{Ni}_{16.6}$ (in at. %). The relative accuracy of the concentration determination was estimated as ± 0.1 at. %.

The diffusion couples were mounted in steel fixtures, sealed in quartz ampules and annealed under purified Ar atmosphere at

1373 K for 48 h. The diffusion couple assembly preparation and details of the radiotracer experiments using the ^{51}Cr , ^{54}Mn , ^{57}Co , ^{59}Fe radioisotopes are identical to those described in our previous report [19]. Additionally, a third augmented tracer-interdiffusion couple experiment was performed in order to investigate Ni diffusion along the interdiffusion zone of this diffusion couple. Since the ^{63}Ni radioisotope, which was available as a HCl solution, is only a β^- -emitter (half-life 101.2 years) it was conveniently analyzed separately using a liquid scintillation counter Tri-Carb 2910 TR by Perkin Elmer.

The composition profiles were measured in EPMA keeping 15 kV acceleration voltage and 50 nA probe current on the identical inactive diffusion couple. Multiple dedicated line-scans perpendicular to the original (Matano) interface between the two end-members were performed using pure elements as standards for all elements. The total scan lengths were set to 500 μm with a step size of 2 μm analyzing approximately 250 μm on each side of the diffusion couple.

2.2. Diffusion simulations

The diffusion simulations were conducted on a continuum scale to recover the experimental time and length scales. As a diffusion model, the pair-diffusion model in formulation for a constant molar volume [24] was applied. It is consistent with the CALPHAD (Calculation of PHase Diagrams) type databases [27]. For all simulations a reliable thermodynamic database [28], especially developed for HEAs, was used.

2.2.1. Pair-diffusion model

The pair-diffusion model [24] treats the diffusion fluxes in a symmetric pair-wise manner. The flux of element i , J_i , in an n -component alloy is defined as:

$$J_i = - \sum_{k=1}^n x_i x_k M_{ik}^p \nabla (\mu_i - \mu_k), \quad (1)$$

where x_i is the mole fraction of element i , M_{ik}^p is the pair-mobility between the elements i and k , and $\nabla (\mu_i - \mu_k)$ is the thermodynamic driving force with μ_i being the chemical potential of an element i . The pair-mobility is the kinetic coefficient for an effective exchange between two elements, which depends on temperature, pressure and the local composition (and it does not implicate any specific diffusion mechanism). The symmetric pair-mobility is defined as:

$$M_{ik}^p = M_i + M_k - \sum_{l=1}^n x_l M_l, \quad (2)$$

where M_i as the atomic mobility of an element i . The composition, temperature and pressure dependence of the atomic mobilities is parameterized and stored in kinetic databases. The pair-mobilities are constructed on-the-fly during the simulations.

As a result, the pair-diffusion coefficients are defined as

$$\tilde{D}_{ij}^p = \sum_{k=1}^n x_i x_k M_{ik}^p \left(\frac{\partial \mu_i}{\partial x_j} - \frac{\partial \mu_k}{\partial x_j} \right), \quad (3)$$

which are equal to the conventional interdiffusion coefficients,

$$\tilde{D}_{ij} = \sum_{k=1}^n (\delta_{ki} - x_i) x_k M_k \frac{\partial \mu_k}{\partial x_j} \quad (4)$$

at the condition that the Gibbs-Duhem relation, i.e. $\sum_k x_k \frac{\partial \mu_k}{\partial x_j} = 0$, is satisfied. This is forced automatically by using the CALPHAD-type definition of thermodynamic factors which we applied in our simulations,

$$\frac{\partial \mu_k}{\partial x_j} = \frac{\partial^2 G_m}{\partial x_k \partial x_j} - \sum_l x_l \frac{\partial^2 G_m}{\partial x_k \partial x_l}, \quad (5)$$

where G_m is the molar Gibbs energy of the alloy.

The diffusion equations were solved using both diffusion coefficients (since the concentrations are nearly equal) without a reference element. This is important for HEA alloys where all elements are equivalent and it is not possible to choose a reference element in a reasonable manner.

2.2.2. CALPHAD-type kinetic databases

Kinetic databases, so-called Diffusion DataBases, DDB-files, contain models and the referring parameters to describe the composition, temperature, and pressure dependence of the atomic mobilities [29]. The main difference between the thermodynamic and kinetic descriptions is that only one Gibbs energy exists for a phase, independent of the number of components. In contrast, n independent atomic mobilities exist in a n component alloy. The composition dependence is modeled as a pyramidal structure, in which the end-member descriptions form the basis. The end-members, in thermodynamics also known as unaries, are pure elements. In the case of atomic mobilities, the term "unaries" is misleading, since not only diffusion of A in A is an end-member ('self-diffusion') but also the mobilities of all other elements in pure A . For example, in a binary A - B system, there are four (kinetic) end-members. In the following, the mobility will be written as $M_{\text{Diffusing Element}}^{\text{Alloy}}$, e.g., A in pure A : M_A^A , A in pure B : M_A^B or A in A - B : M_A^{AB} .

The end-member parameterization is described with the Arrhenius laws [30,31]:

$$M_i^k = \exp\left(\frac{RT \ln M_i^{k,0}}{RT}\right) \exp\left(-\frac{Q_i^{k,a}}{RT}\right) \frac{1}{RT}, \quad (6)$$

where R is the ideal gas constant, T the temperature, $M_i^{k,0}$ the frequency factor and $Q_i^{k,a}$ is the activation enthalpy for diffusion of i in an alloy k . This term can be extended to account for magnetic and ordering phenomena, which is described in detail in Ref. [31]. It was found that $M_i^{k,0}$ is only slightly concentration dependent and thus the whole composition dependence is evaluated within $Q_i^k = RT \ln M_i^{k,0} - Q_i^{k,a}$ using Redlich-Kister polynomials and their extension to quaternary interactions [32–34]:

$$Q_i^k = \sum_{p=1}^n x_p Q_i^p + \sum_p \sum_{q>p}^n x_p x_q \left[\sum_{r=0}^m A_i^{pq,r} (x_p - x_q)^r \right] + \sum_p \sum_{q>p}^n \sum_{v>q}^n x_p x_q x_v [v_{pqv}^s B_i^{pqv,s}]. \quad (7)$$

The first term describes the interpolation between the end-members, the second term adds binary interaction terms with the fitting parameters $A_i^{pq,r}$, where p and q are the interacting elements and r is the order. The last term describes the ternary interactions, following the symmetric thermodynamic approach with $v_{pqv}^s = x_s + \frac{(1-x_p-x_q-x_v)}{3}$, $s \in (p, q, v)$. The ternary interaction parameters, $B_i^{pqv,s}$, describe the influence of the interactions between p , q and v on diffusion of element i . Within the pyramidal description, the end-member terms are assessed first, based on this the binary parameters are added and finally the ternary parameters are evaluated.

The parameters of the models are assessed with the help of measured or calculated kinetic data (the tracer diffusion coefficients D_i^* , interdiffusion coefficients \tilde{D}_{ij} and intrinsic diffusion coefficients D_{ij}).

2.3. Relations between the interdiffusion, intrinsic- and tracer diffusion coefficients

In the context of multi-component interdiffusion, the interdiffusion flux (\tilde{J}_i) of a component i is related to the interdiffusion coefficients and the concentration gradients by [35].

$$\tilde{J}_i = -\sum_{j=1}^{n-1} \tilde{D}_{ij}^n \frac{\partial C_j}{\partial y} = -\frac{1}{V_m} \sum_{j=1}^{n-1} \tilde{D}_{ij}^n \frac{\partial x_j}{\partial y}, \quad (8)$$

where $\left(\frac{\partial C_j}{\partial y}\right)$ is the concentration gradient of the component j , V_m is the molar volume. x_j is the composition (mole fraction) of the element j . \tilde{D}_{ij}^n is the main interdiffusion coefficient of the component i and it is related to its own concentration gradient. \tilde{D}_{ij}^n are the cross interdiffusion coefficients and they are related to the concentration gradients of the components j . The component n is considered as a dependent component as per Onsager formalism [36]. Interdiffusion coefficients without the reference element n are given in Eq. 4 and these are related by

$$\tilde{D}_{ij}^n = \tilde{D}_{ij} - \tilde{D}_{in} \quad (9)$$

Kirkaldy and Lane [37] derived an expression relating the interdiffusion coefficients to the intrinsic diffusion coefficients,

$$\tilde{D}_{ij}^n = D_{ij}^n - x_i \left(\sum_{k=1}^n D_{kj}^n \right), \quad (10)$$

where D_{ii}^n is the main intrinsic diffusion coefficient, D_{ij}^n are the cross intrinsic diffusion coefficients. Kirkaldy and Lane have shown that the tracer diffusion coefficients can be indirectly estimated from the results of the diffusion couple measurements [37]. Below, we show how to extract the interdiffusion coefficients in the context of the tracer-interdiffusion couple experiments.

Accounting for the vacancy wind effect in a multi-component system [22,38], the intrinsic diffusion coefficients are related to the tracer diffusion coefficients,

$$D_{ij}^n = \frac{x_j}{x_i} D_i^* \phi_{ij}^n (1 + W_{ij}^n), \quad (11)$$

where $D_i^* = RTM_i$ are the tracer diffusion coefficients which are measured experimentally and the vacancy wind factors are [38].

$$W_{ij}^n = \frac{2}{S_0 \phi_{ij}^n} \frac{\sum_{k=1}^n x_k D_k^* \phi_{kj}^n}{\sum_{k=1}^n x_k D_k^*}. \quad (12)$$

Here, the thermodynamic factors (ϕ_{ij}^n) are calculated from the chemical potential gradients using the thermodynamic database developed in [24,28],

$$\phi_{ij}^n = \frac{x_j}{RT} \left(\frac{\partial \mu_i}{\partial x_j} - \frac{\partial \mu_i}{\partial x_n} \right). \quad (13)$$

3. Results and discussions

3.1. Interdiffusion measurements

Fig 1 (a) shows the averaged and smoothed concentration profiles of all constituting elements measured by multiple dedicated line-scans for the Co-17/23 couple using the EPMA technique. The smoothed profiles are normalized by the sum of the element concentrations at each point to achieve $N_T = 1$ throughout the interdiffusion zone, and once again the continuity of the profiles was verified after normalization. The origin of the depth coordinate y is set at the position of the Matano plane [39] of Ni. The Matano plane position parameter (y_m) is identified using

$$y_m = \frac{\int_{C_i^-}^{C_i^+} y dC_i}{C_i^+ - C_i^-} \quad (14)$$

where C_i^- (C_i^+) denotes the concentration on the left-hand (right-hand) side. The Matano plane of Co is shifted by about 12 μm to the left from the Matano plane of Ni. The reason for this could be the appearance of minor up-hill diffusion in the Co concentration profile at about 50 μm and the variation of the molar volume along the

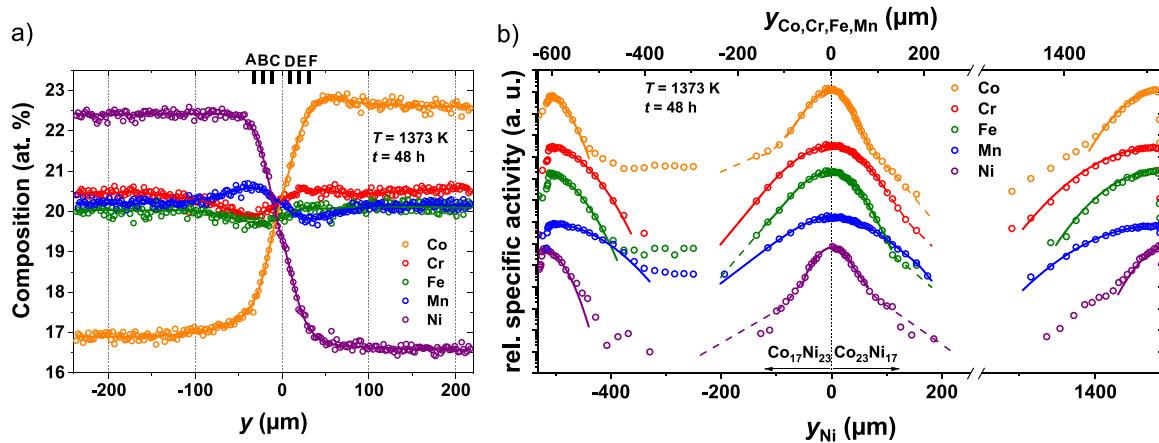


Figure 1. (a) Composition profile measured in EPMA; (b) the tracer penetration profiles determined by the tracer/interdiffusion couple approach (open symbols, the volume and grain boundary diffusion contributions to the tracer transport are distinguished by solid and dashed lines, respectively). In (a), A–F indicate the compositions for which the element fluxes are determined to check the consistency of tracer and chemical diffusion coefficients. In (b), the tracer profiles are shifted along the ordinate axis for a better readability. Since two physically different (but identical) couples were used for tracer diffusion measurements using the Ni and Co+Cr+Fe+Mn isotopes, two different abscissa axes are used (the type of the corresponding tracer is indicated by subscripts).

diffusion path is also not known to us. Smoothing of this small up-hill effect to a constant concentration would shift the Matano plane of Co to a position similar to Ni within the experimental uncertainties.

Similar to the case of the Co-15/25 diffusion couple [19], Fig. 1 (a) reveals that Co-17/23 is a non-ideal pseudo-binary couple [2] as well. In the nominally $\text{Co}_{23}\text{CrFeMnNi}_{17}$ and $\text{Co}_{17}\text{CrFeMnNi}_{23}$ alloys, the Co, Cr, Mn and Ni concentrations deviate by less than 0.6 at.% from their nominal values. Moreover, the appearance of up-hill diffusion in the concentration profiles of the nominally equiatomic constituents, i.e. of Cr, Fe and Mn, is confirmed, too. In the Co-17/23 diffusion couple, Cr and Mn show distinct up-hill diffusion deviating by about 0.5 at.% from the equiatomic compositions to the opposite directions, like in the Co-15/25 couple. Here, the appearance of the up-hill diffusion effect may probably be explained by accounting for the competition between different atomic species with respect to vacancies, as it was proposed for the Co-15/25 couple [19]. A comparably smaller deviation of the up-hill concentration from the equiatomic one may correlate with a smaller concentration gradient of Co and Ni in comparison to the previously analyzed diffusion couple.

3.2. Tracer diffusion measurements

Fig. 1 (b) shows the measured penetration profiles for ^{57}Co , ^{51}Cr , ^{59}Fe , ^{54}Mn and ^{63}Ni diffusion in the Co-17/23 couple. For a better readability, the tracer profiles are relatively shifted along the ordinate axis. Since two separate augmented tracer-interdiffusion experiments were performed, namely one with the ^{63}Ni radioisotope and one with a mixture of the ^{57}Co , ^{51}Cr , ^{59}Fe , and ^{54}Mn isotopes, the origin of both abscissa axes is set at the Matano interface positions of the corresponding diffusion couples (the top y-coordinate in Fig. 1 (b) corresponds to the Co, Cr, Fe and Mn penetration profiles, the bottom one is related to the Ni penetration profile). A few factors might contribute to a certain misalignment between the y-scales for the interdiffusion and tracer diffusion concentration profiles (Fig. 1 (a) and (b)): .

- final accuracy of the sample's thickness measurements;
- non-propagating error of the thickness determination of each individual section;

- accuracy of the sample orientation for the mechanical grinding perpendicular to the diffusion direction;
- accuracy of the positioning of line scan perpendicularly to the Matano plane.

The total accuracy of the length measurements in the tracer experiment can conservatively be estimated to be less than 1%.

Comparing the length scales in Fig. 1 (a) and (b) we conclude that the tracer penetration profiles measured in end-members (outer profiles) are located in regions without any influence of a chemical driving force. Thus, these profiles correspond to tracer diffusion in the unaffected (homogeneous) end-members and therefore they can be analyzed using the thin film solution of the diffusion problem [39].

$$C_i^*(y, t) = \frac{M_i}{\sqrt{\pi D_i^* t}} \exp\left(-\frac{(y - y_0)^2}{4 D_i^* t}\right). \quad (15)$$

Here, M_i denotes the initial amount of the tracer i , C_i^* the tracer concentration of the tracer i in the layer (which is proportional to the relative specific activity of the tracer), y_0 denotes the origin of the diffusion source, i.e. the left or the right end of the diffusion couple, D_i^* is the corresponding volume diffusion coefficient, and t is the diffusion time.

The penetration profiles follow the thin film solution over about three orders of magnitude revealing the existence of a further (fast-diffusion) branch. Those branches were attributed to grain boundary diffusion as it was seen in our previous work on diffusion in polycrystalline CoCrFeMnNi HEAs [12,13,19]. In the present work, the grain boundary diffusion contributions in the unaffected end-members (as well as in the interdiffusion zone) are neglected, since we are focused on the volume diffusion branches. The solid lines in the unaffected end-members in Fig. 1 (b) represent the fits according to the Gaussian solutions, Eq. (15). The tracer penetration profiles measured for left end-members show near-surface features with conspicuous maxima at about -600 (Co, Cr, Fe and Mn tracers, upper axis) or $-500 \mu\text{m}$ (Ni tracer, bottom axis). These deviations from the Gaussian-type solutions, Eq. (15), are due to a direct contact with the Ta foil, small and irregular pieces of which occurred to be stuck to the sample surface after annealing and affected the first few sections. The maxima correspond to the positions at which the whole

Table 1

Tracer volume diffusion coefficients, D_i^* , measured for the Co-17/23 diffusion couple at 1373 K in the unaffected end-members. The uncertainty of the D_i^* values is typically below 20%. For comparison the tracer volume diffusion coefficients, D_i^* , measured for the Co-15/25 diffusion couple HEA at 1373 K in the unaffected end-members [19] and the averaged tracer diffusion coefficients determined for single-crystalline equiatomic CoCrFeMnNi HEAs [14,15] are listed, too.

Alloy	Co D_i^* (10^{-15} m ² s ⁻¹)	Cr	Fe	Mn	Ni	Ref.
Co ₂₃ CrFeMnNi ₁₇	1.8 ± 0.4	4.3 ± 0.9	2.7 ± 0.5	5.4 ± 1.1	1.4 ± 0.3	present work
Co ₁₇ CrFeMnNi ₂₃	2.0 ± 0.4	5.3 ± 1.1	4.2 ± 1.1	11.0 ± 2.2	1.3 ± 0.3	present work
Co ₂₅ CrFeMnNi ₁₅	1.2 ± 0.1	3.9 ± 0.1	2.4 ± 0.1	8.2 ± 0.2	–	[19]
Co ₁₅ CrFeMnNi ₂₅	2.1 ± 0.1	5.6 ± 0.1	4.2 ± 0.1	13.3 ± 0.6	–	[19]
CoCrFeMnNi	1.9 ± 0.2	5.0 ± 0.6	3.4 ± 0.5	9.0 ± 1.0	1.2 ± 0.3	[14,15]

sample surface (without Ta residuals) was sectioned. Therefore, the data points on the left hand side of the maxima were not included in the analysis. However, the Gaussian solutions were found to hold safely for the deeper sections. The usage of an exact solution for the diffusion problem accounting for a tracer evaporation provided by Crank [40], which would mimic the present situation, was found to result in the same value of the diffusion coefficients within the given experimental uncertainties.

Table 1 provides the bulk diffusion coefficients in the unaffected end-members of the Co-17/23 couple compared to the bulk diffusion coefficients in the unaffected end-members of the Co-15/25 couple [19] and to the bulk diffusion coefficients in the equiatomic counterparts measured in single-crystalline CoCrFeMnNi [14,15]. The bulk diffusion coefficients of all elements are found to be in a good agreement within the experimental uncertainties, with Mn being the fastest diffusing element in all compositions followed by Cr, whereas Ni represents the slowest diffusing element with the diffusion rates slightly below those of Co. In the Ni-enriched alloy, the diffusion coefficients of Cr and Fe are found to be up to 55% higher than in the Co-enriched alloy and Mn shows even 100% faster rates. In contrast to this behavior, the diffusion rates of Co and Ni are found to be approximately constant in both parts of the couple within the experimental uncertainties. In the equiatomic composition, the diffusion rates of Cr, Fe and Mn are found to be in-between the corresponding diffusion coefficients, D_i^* estimated in the unaffected end-members of Co₁₇CrFeMnNi₂₃ and Co₂₃CrFeMnNi₁₇, whereas the diffusion rates of Co and Ni in single-crystalline CoCrFeMnNi correspond perfectly to the values estimated in the unaffected end-members under consideration of the experimental uncertainties.

Grain boundary diffusion contributions are clearly seen for the tracer penetration profiles, especially for Co and Ni, Fig. 1 (b). As a rule of thumb, in coarse-grained polycrystalline materials the grain boundary contributions are clearly distinguishable at depths larger than about $(2-5) \times \sqrt{D_i^* t}$, where D_i^* is the corresponding tracer bulk diffusion coefficient of the element i [35]. Since Mn and Cr are diffusing relatively fast, the corresponding contributions would be distinguishable if we would follow their diffusion to larger depths, which was not the aim of the present study. While the current tracer profiles are insufficient to generate reliable grain boundary diffusion data for all alloying elements, we exempted the short-circuit contributions from our analysis and discussion.

3.3. Estimation of tracer diffusion coefficients under concentration gradient

The penetration profiles in the interdiffusion zone were analyzed using the solution for the thin layer isotope sandwich configuration, [17].

$$D_i^* = - \left(\frac{(y+a)}{2t} + \frac{\tilde{J}_i}{C_i} \right) / \left(\frac{\partial \ln C_i^*}{\partial y} - \frac{\partial \ln C_i}{\partial y} \right). \quad (16)$$

Here, D_i^* is the tracer diffusion coefficients of the element i , C_i is the concentration of the element i , C_i^* is the tracer concentration of the element i in the interdiffusion zone, \tilde{J}_i is the interdiffusion flux of the element i , determined using the Sauer-Freise approach [41],

$$\tilde{J}_i = - \frac{C_i^* - C_i^-}{2t} \left[(1 - Y_i^*) \int_{y^-}^{y^*} Y_i dy + Y_i^* \int_{y^*}^{y^+} (1 - Y_i) dy \right] \quad (17)$$

where, $Y_i = (C_i - C_i^-)/(C_i^* - C_i^-)$. Since the molar mass is estimated to be practically constant for the composition range, the Sauer-Freise approach is a reasonable approximation. The parameter a accounts for the misfit of the y scales for the chemical, C_i , and the tracer, C_i^* , profiles of the element i [16]. The value of the parameter a in Eq. (16) is optimised in an iterative manner to obtain a monotonous composition dependence of the tracer diffusion coefficient D_i^* [17,19]. In Fig. 1 (b), the solid and dashed lines indicate the bulk and grain boundary diffusion contributions, respectively.

The estimated concentration-dependent tracer diffusion coefficients are shown in Fig. 2 (a), solid lines. Moreover, we re-analyzed the complete tracer concentration profiles in the interdiffusion zone measured in the Co-15/25 couple [19] and these data are also shown in Fig. 2 (a) using dashed lines. In good agreement with the previous findings on equiatomic single-crystalline CoCrFeMnNi [14,15], Mn is the fastest diffusing element in the alloys followed by Cr at $T = 1373$ K, whereas Ni represents the slowest diffusing element comparable to Co.

The tracer diffusion coefficients of the constituent elements in the nearly equiatomic CoCrFeMnNi system depend differently on the alloy composition. With increasing Co content from 15 to 25 at.%, the diffusion coefficients of Co, Fe and Ni decrease by a factor of two. The Mn diffusivity decreases most significantly and the Cr diffusion coefficient remains almost constant.

As a remarkable feature, one recognizes a good agreement of the bulk diffusion coefficients obtained from the unaffected end-members with the independently measured diffusion coefficients under chemical gradients along the diffusion path, Fig. 2 (a). Furthermore, within the experimental uncertainties the end-member coefficients of the Co₁₇CrFeMnNi₂₃ and Co₂₃CrFeMnNi₁₇ alloys also agree with the diffusion coefficients along the diffusion path corresponding to the Co-17/23 couple. Small deviations from the established trends might be indicated for Cr and Ni in the Co₁₇CrFeMnNi₂₃ alloy. Taking the bulk diffusion coefficients of the constituents in the equiatomic state into account, the tracer diffusion coefficients of Co, Fe, Mn and Ni along the diffusion path agree with the corresponding independently measured coefficients in the single-crystalline CoCrFeMnNi HEA [14,15]. Cr represents one exception in this case, however, the Cr value in an equiatomic state is exactly in-between the coefficients along the diffusion paths.

Some minor differences are seen between the tendencies established for the Co-15/25 and Co-17/23 couples. For example, Fe reveals almost similar trends while the dependence of the Co diffusion coefficient on the composition near the equiatomic one is opposite for the two couples. Alongside with usual experimental uncertainties, one has to highlight a (relatively minor) difference in

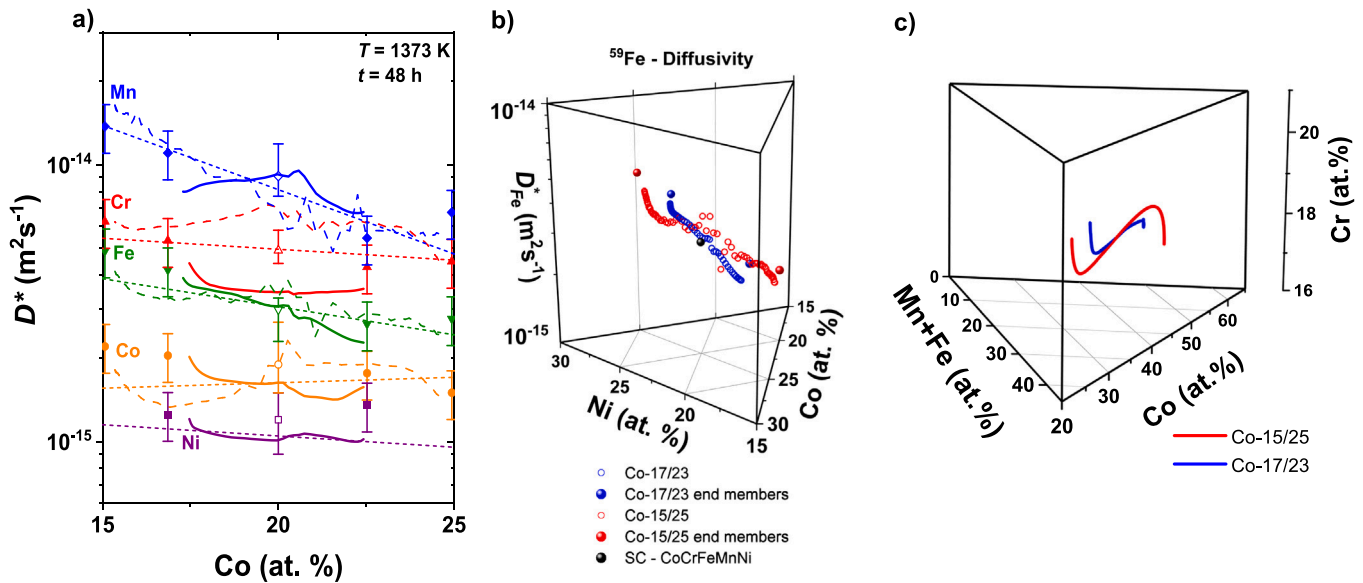


Figure 2. a) Comparison of the concentration-dependent tracer diffusion coefficients measured for the Co-15/25 (dashed lines) and Co-17/23 (solid lines) couples. The filled symbols correspond to the bulk diffusion coefficients measured in the unaffected end-members of each alloy [19], whereas the open symbols represent the bulk diffusion coefficient of the constituents in single crystalline equiatomic CoCrFeMnNi [14,15]. The dotted lines represent the averaged trends. b) the ^{59}Fe diffusion coefficients as function of composition on the ternary diagram Co–Ni–(Cr+Fe+Mn) measured for the Co-15/25 (open red symbols) and Co-17/23 (open blue symbols) couples, for the unaffected end-members (filled symbols) and in single crystalline equiatomic CoCrFeMnNi HEA (black symbol) [14]. c) the diffusion paths developed along the composition profiles displayed on the Quaternary diagram Co–Ni–(Mn+Fe)–Cr.

Table 2

The compositions along the diffusion path in Co-17/23 diffusion couple chosen to estimate the interdiffusion coefficients.

Element (at%)	A	B	C	D	E	F
Co	17.75	18.33	19.23	20.91	21.69	22.27
Cr	19.90	19.96	20.09	20.37	20.46	20.52
Fe	19.74	19.73	19.76	19.92	20.03	20.08
Mn	20.59	20.54	20.41	20.03	19.91	19.85
Ni	22.02	21.44	20.51	18.77	17.91	17.28

the diffusion paths developed in the two couples due to the different magnitudes of up-hill diffusion for Cr and Mn. In fact, Fig. 2(c) clearly indicates that the diffusion paths of these two couples (Co-15/25 and Co-17/23) are close to each other but do not overlap exactly. This is a well known behavior in multi-component diffusion that the diffusion paths are strongly influenced by the exact end-member compositions [42].

In Fig. 2 (b), the Fe tracer diffusion coefficients are plotted as function of composition on the triangle Ni–Co–(Cr+Fe+Mn). The tracer diffusion coefficients measured both for the interdiffusion zones (open symbols) and for the corresponding end-member compositions (closed symbols) are shown. The Fe bulk diffusion coefficient measured in single-crystalline equiatomic CoCrFeMnNi [14] at 1373 K is represented by the black symbol. With the chosen representation, the developed composition profiles as well as the measured diffusion coefficients are similar.

3.4. Estimation of interdiffusion coefficients in tracer/interdiffusion couple method

The estimation of the intrinsic and interdiffusion coefficients by the augmented tracer/interdiffusion couple method is demonstrated for the first time in this work. The tracer diffusion coefficients estimated from this approach and the thermodynamic parameters calculated from the database developed from the previous work [24] is utilized for this calculation. Specific compositions along the

developed diffusion path in the interdiffusion zone are chosen, these are indicated in Fig. 1 and the chosen compositions are listed in the Table 2.

To demonstrate the validity of this approach, the composition B from Table 2 is considered here in detail; data for the other compositions are tabulated in Appendix, Tables A2, A3, A4, and A5. First, the thermodynamic factors are calculated for the given composition, these are calculated using Eq. (13) utilizing the chemical potential gradients extracted from the thermodynamic database developed from this study [24,28]. The vacancy wind factors were calculated using Eq. (12). To calculate vacancy wind factors, the estimated tracer diffusion coefficients measured along the diffusion paths are considered here. Further, combining tracer diffusion coefficients, thermodynamic factors and the vacancy wind factors we can estimate the intrinsic diffusion coefficients by using Eq. (11). Now, from the known intrinsic diffusion data we can calculate the interdiffusion coefficients following Eq. (10). The intrinsic and interdiffusion coefficients estimated are listed in Table 3 along with other relevant diffusion parameters.

Fig. 3 represents the interdiffusion fluxes of the elements calculated directly from the composition profiles of the diffusion couple as shown in Fig. 1(a) using the Eq.(17). Note that the composition profiles are given in atomic percentage and we have assumed a constant molar volume ($6.85 \times 10^{-6} \text{ m}^3/\text{mol}$), since the changes of the molar volume are found to be negligible in the vicinity of the equiatomic composition, according to our XRD data [19]. The directly estimated interdiffusion fluxes from the composition profiles can be compared with the interdiffusion fluxes calculated from interdiffusion coefficients (as explained above) using the composition gradients from the composition profiles by applying Eq. (8). Positions of the individual compositions chosen for the estimation of the interdiffusion coefficients are also denoted as A, B, C, D, E and F as it was listed in the Table 2. At these compositions, the interdiffusion fluxes are then calculated for the individual elements and shown in Fig. 3 for comparison. The mismatch is acceptable considering three different types of experiments, uncertainty in extracted thermodynamic factors and the different fitting and smoothening of tracer

Table 3

Thermodynamic factors (ϕ_{ij}^{Ni}), vacancy wind factors ($1 + W_{ij}^{Ni}$), intrinsic diffusion coefficients (D_{ij}^{Ni}) and interdiffusion coefficients (\tilde{D}_{ij}^{Ni}) estimated at the composition B considering Ni as dependent component.

ϕ_{ij}^{Ni}		$1 + W_{ij}^{Ni}$		D_{ij}^{Ni}	($\times 10^{-15}$ m ² /s)	\tilde{D}_{ij}^{Ni}	($\times 10^{-15}$ m ² /s)
ϕ_{CoCo}^{Ni}	1.0089	$1 + W_{CoCo}^{Ni}$	1.0222	D_{CoCo}^{Ni}	1.7251	\tilde{D}_{CoCo}^{Ni}	1.3334
ϕ_{CoCr}^{Ni}	-0.4215	$1 + W_{CoCr}^{Ni}$	0.7480	D_{CoCr}^{Ni}	-0.4843	\tilde{D}_{CoCr}^{Ni}	-2.1465
ϕ_{CoFe}^{Ni}	-0.2457	$1 + W_{CoFe}^{Ni}$	0.6660	D_{CoFe}^{Ni}	-0.2543	\tilde{D}_{CoFe}^{Ni}	-1.5533
ϕ_{CoMn}^{Ni}	-0.4002	$1 + W_{CoMn}^{Ni}$	0.4804	D_{CoMn}^{Ni}	-0.2870	\tilde{D}_{CoMn}^{Ni}	-3.4491
ϕ_{CrCo}^{Ni}	-0.2045	$1 + W_{CrCo}^{Ni}$	0.8907	D_{CrCo}^{Ni}	-0.7159	\tilde{D}_{CrCo}^{Ni}	-1.0838
ϕ_{CrCr}^{Ni}	0.9697	$1 + W_{CrCr}^{Ni}$	1.1095	D_{CrCr}^{Ni}	3.8830	\tilde{D}_{CrCr}^{Ni}	2.0728
ϕ_{CrFe}^{Ni}	-0.0670	$1 + W_{CrFe}^{Ni}$	-0.2246	D_{CrFe}^{Ni}	0.0549	\tilde{D}_{CrFe}^{Ni}	-1.3597
ϕ_{CrMn}^{Ni}	0.2393	$1 + W_{CrMn}^{Ni}$	1.8690	D_{CrMn}^{Ni}	1.5686	\tilde{D}_{CrMn}^{Ni}	-1.8753
ϕ_{FeCo}^{Ni}	-0.0547	$1 + W_{FeCo}^{Ni}$	0.5915	D_{FeCo}^{Ni}	-0.1211	\tilde{D}_{FeCo}^{Ni}	-0.5428
ϕ_{FeCr}^{Ni}	-0.0776	$1 + W_{FeCr}^{Ni}$	-0.3688	D_{FeCr}^{Ni}	0.0984	\tilde{D}_{FeCr}^{Ni}	-1.6914
ϕ_{FeFe}^{Ni}	1.0024	$1 + W_{FeFe}^{Ni}$	1.0819	D_{FeFe}^{Ni}	3.7725	\tilde{D}_{FeFe}^{Ni}	2.3738
ϕ_{FeMn}^{Ni}	0.0182	$1 + W_{FeMn}^{Ni}$	12.4438	D_{FeMn}^{Ni}	0.7568	\tilde{D}_{FeMn}^{Ni}	-2.6491
ϕ_{MnCo}^{Ni}	0.1997	$1 + W_{MnCo}^{Ni}$	1.1119	D_{MnCo}^{Ni}	2.1638	\tilde{D}_{MnCo}^{Ni}	1.7256
ϕ_{MnCr}^{Ni}	0.6401	$1 + W_{MnCr}^{Ni}$	1.1659	D_{MnCr}^{Ni}	6.6787	\tilde{D}_{MnCr}^{Ni}	4.8162
ϕ_{MnFe}^{Ni}	0.4302	$1 + W_{MnFe}^{Ni}$	1.1908	D_{MnFe}^{Ni}	4.6380	\tilde{D}_{MnFe}^{Ni}	3.1806
ϕ_{MnMn}^{Ni}	1.7096	$1 + W_{MnMn}^{Ni}$	1.1216	D_{MnMn}^{Ni}	16.6754	\tilde{D}_{MnMn}^{Ni}	13.1319
ϕ_{NiCo}^{Ni}	-0.8132	$1 + W_{NiCo}^{Ni}$	0.9725	D_{NiCo}^{Ni}	-0.9744	-	-
ϕ_{NiCr}^{Ni}	-1.0843	$1 + W_{NiCr}^{Ni}$	0.9020	D_{NiCr}^{Ni}	-1.1067	-	-
ϕ_{NiFe}^{Ni}	-1.0624	$1 + W_{NiFe}^{Ni}$	0.9228	D_{NiFe}^{Ni}	-1.1222	-	-
ϕ_{NiMn}^{Ni}	-1.5353	$1 + W_{NiMn}^{Ni}$	0.8646	D_{NiMn}^{Ni}	-1.4596	-	-

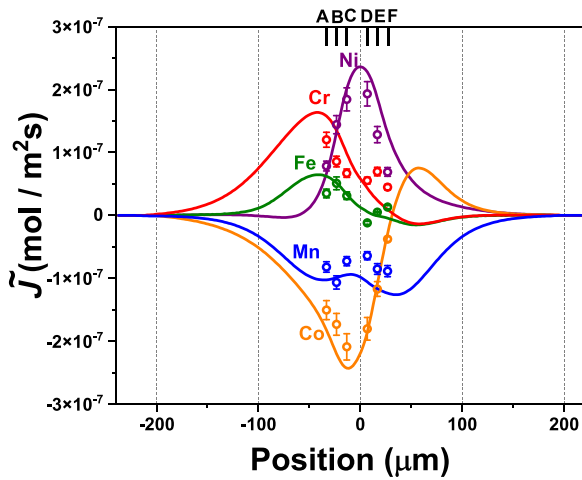


Figure 3. Comparison of the interdiffusion fluxes calculated from the composition profiles directly (solid lines) with those calculated as a product of the interdiffusion coefficients, which are estimated via the independently determined tracer diffusion coefficients, thermodynamic factors and the vacancy wind factors, Eqs. (10)–(13), and the corresponding composition gradients (symbols). The comparison is done for six compositions marked sequentially from A to F.

and composition profiles of the components. These calculations highlight the reliability of the estimation of all types of diffusion parameters following the experimental method proposed in this study.

3.5. Simulation results

Concentration profiles corresponding to interdiffusion and tracer diffusion in the Co-17/23 diffusion couple were calculated using the

thermodynamic database developed by [28] and improved in our paper related to the diffusion couple Co-15/25 [24]. This improvement allows reproduction of the experimental profiles for Mn and Cr diffusion in the Co-15/25 couple much better than in the previous work [19]. The mobilities were calculated using the exponential dependencies on the Co concentration which were obtained by linear fitting of the tracer diffusion coefficients measured in the experiment shown in Fig. 2 (a). For the fitting, the following dependency is chosen,

$$\ln(D^*) = a(x - x_0) + b, \quad \text{or} \quad M = \frac{1}{RT} \exp(a(x - x_0) + b). \quad (18)$$

Here a and b are the fitting parameters listed in Table 4, and $x_0 = 0.2$ is the mole fraction of Co at the Matano plane, where all concentrations are equal to 0.2. The coefficient $b = \ln(D^*(x_0))$ defines the tracer diffusion coefficients at this mean point. The linear dependencies are chosen as a simplest form of the CALPHAD-type dependency Eq.(7). This can be reasonable for a short concentration region, where the tracer diffusion coefficients were measured. The dependencies can be useful for the assessment of the mobility parameters and the consistent development of the mobility database. The fitting is done by two methods: using all measured points and using only end-member values.

An extrapolation of any dataset is an extremely delicate Ansatz. We used the CALPHAD-type mobility representation and developed the parameters accordingly to describe adequately diffusion for about equiatomic compositions. A development of a full kinetic database for the CoCrFeMnNi system (including pure elements and all other sub-systems) is straightforward, but out of scope of the present paper.

The parameters obtained by end-member points in the couple Co-15/25 are closer to the parameters in the couple Co-17/23 obtained by the fitting of all measured points and also are close to the dependencies obtained in the previous work [19]. The deviations are

Table 4

Parameters of the linear fitting of tracer diffusion coefficients for all measured points and for end-members.

Couple Element	For all measured points				For end-members			
	Co-17/23		Co-15/25		Co-17/23		Co-15/25	
	<i>a</i>	<i>b</i>	<i>a</i>	<i>b</i>	<i>a</i>	<i>b</i>	<i>a</i>	<i>b</i>
Co	-4.896	-34.068	1.667	-34.040	-2.592	-33.904	3.903	-33.940
Cr	-2.832	-33.258	-1.216	-32.766	-3.894	-32.988	-3.364	-32.874
Fe	-9.727	-33.458	-3.808	-33.403	-7.941	-33.360	-5.714	-33.235
Mn	-3.058	-32.459	-1.198	-32.417	12.495	-32.531	-7.239	-31.951
Ni	-1.877	-34.492	-	-	1.379	-34.270	-	-

within typical experimental uncertainties, though the diffusion paths are slightly different, Fig. 2(c). In the simulations, we have used the fitting of all measured points in the couple Co-17/23. Note here that the Ni tracer diffusion data were not measured for the Co-15/25 couple.

The simulations were carried out over the domain of 600 μm with the grid size of $\Delta y = 1\mu\text{m}$ and using the time step of $\Delta t = 5\text{ s}$. All five diffusion equations were solved for five components.

The initial concentration profiles are calculated using the erf-function:

$$x_i = \frac{(x_i^+ + x_i^-)}{2} + \frac{(x_i^+ - x_i^-)}{2} \operatorname{erf}\left(\frac{y}{2}\right), \quad (19)$$

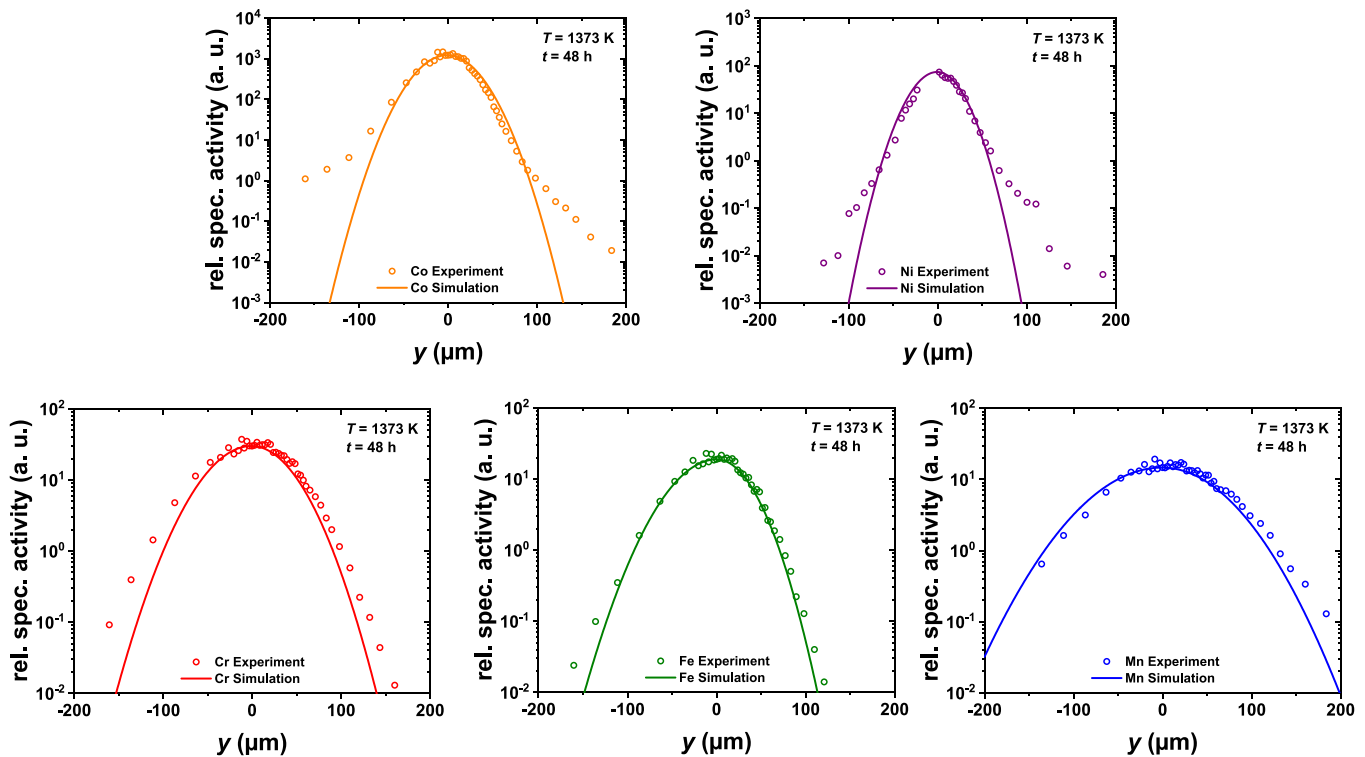
where y is the grid point in micrometers, $x_i^-(x_i^+)$ is the mole fractions on the left (right) side of the diffusion couple. The initial profiles were smoothed to simplify the finite difference numerical computation scheme and to avoid extremely large concentration gradients during the first time iterations (the initial profile broadening was artificially set to 2 μm). Moreover, such a procedure reflects the experimental determination of the chemical profiles using EPMA. The excited volume is about μm^3 and one cannot measure an ideal step function. In

addition, it is almost impossible to produce atomically flat end members for diffusion couple experiment. The initial concentrations used in the simulations are $x_i^- = \{0.16899, 0.20443, 0.20037, 0.20210\}$ and $x_i^+ = \{0.22600, 0.20578, 0.20096, 0.20151\}$ for Co, Cr, Fe, Mn, respectively.

To calculate the tracer diffusion profiles, the initial tracer profiles for all elements were added with the center at the Matano plane, $y = 0$, using the Gaussian distribution,

$$x_i^* = 0.1 \frac{0.2}{\sqrt{\pi}4} \exp\left(-\frac{y^2}{4}\right). \quad (20)$$

Here, the factor 0.2 is responsible for an equiatomic mixture of the tracer isotopes and the factor 0.1 is the re-normalization of the experimental thickness of the tracer layer (100 nm) to the simulation grid size. This procedure allows to keep the sum of all mole fractions constant. Again, to avoid numerical problems with large gradients, the broadening of the initial profiles was set to 2 μm . Note that a reduction of the broadening along with a corresponding reduction of the discretization size does not affect the resulting profiles.

**Figure 4.** Comparison between the experimentally measured and simulated tracer diffusion profiles in the interdiffusion zone in Co-17/23 at 1373 K after 48 h.

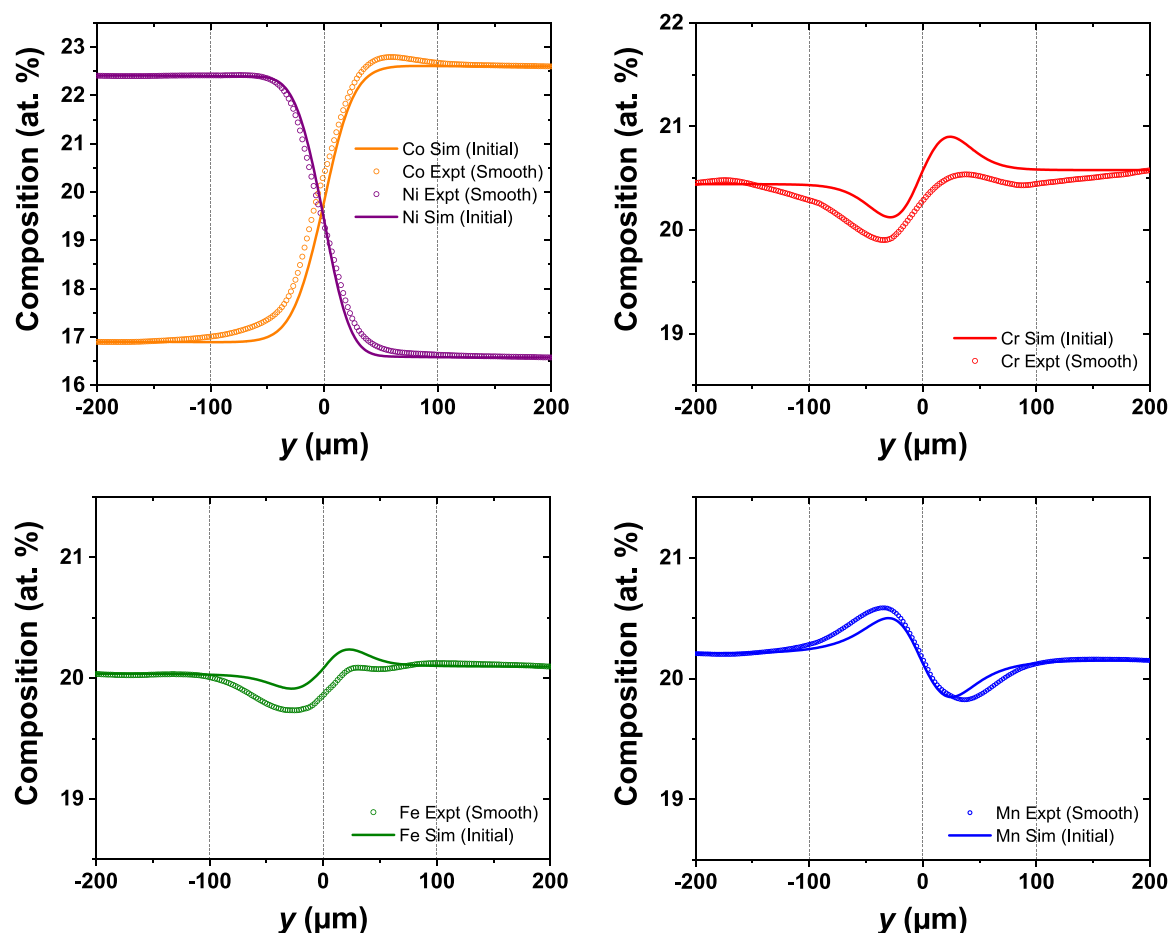


Figure 5. Comparison between the experimental and simulated interdiffusion profiles in Co-17/23 at 1373 K after 48 h.

The comparison of the tracer simulation results with the experiment is shown in Fig. 4. The agreement is very reasonable. The mobility of Cr seems to be a little bit underestimated on the left side with a smaller Co concentration. The mobilities of Ni and Mn are vice versa overestimated on the left side. This behavior can be also caused by other components, which are not taken into account in the linear fitting Eq. (18).

The comparison of the simulated interdiffusion profiles with the experiment is shown in Fig. 5. The mole fractions are recalculated to at.%. As it can be observed in the plots, the simulation cannot reproduce an excess of the Co concentration (Co up-hill) and a decrease of Fe and Cr concentrations near the Matano plane. The Ni and Mn concentrations have an agreement with the experiment at a tolerable level. It is interesting that the up-hill on the Co profile was not observed in the couple Co-15/25. Moreover, the simulation results in this couple reproduced very well the experimental profiles [24]. There is also no reason to suspect that the thermodynamic data can be different for Co-15/25 and Co-17/23 couples.

The experimental diffusion profiles in Fig. 5, especially those of Co, Cr and Fe, provide an impression of a violation of the mass conservation during interdiffusion. Although the profiles are presented in mole fractions rather than correspond to actual numbers of atoms, accounting for different molar volumes of the components does not affect the calculated profiles, as it was already mentioned. Hereto, two aspects have to be discussed. Firstly, the exact concentrations of Mn, Cr and Fe are not the same for the two end-

members, that affects the integration of the composition profiles to determine the Matano position, Eq. (14).

Secondly, there is an issue with the experimental identification of the Matano plane position in a multicomponent system by following Eq. (14), see e.g. Ref. [43]. The Matano plane positions determined for different elements can differ by more than 80 μm [43]. In the present case, Cr shows the maximum deviation for the Matano plane position from that for Ni, about 30 μm . Note that in Fig. 5, the Matano plane determined for Ni was used as the origin of the abscissa.

The simulated profile of Co shown in Fig. 5 underestimates constantly the experimentally measured Co profile. This is due to the Matano plane position identification issue. Though, this is only a representation issue in our case. The exact location of the Matano plane does not enter the present analysis and the tracer diffusion coefficients are determined reliably.

An extended analysis has shown that the appearance of a minor Co up-hill diffusion behavior, Fig. 6, might be explained by some residual heterogeneity of the chemical composition in the end-members. Whereas a pre-existing 'bump' of Co concentration might develop to the extent which would match perfectly the experimental profile, a local increase of the Ni concentration will disappear. Such a behavior is closely related to the different signs of the cross terms of the interdiffusion matrix, see Table 3.

However, the exact nature of the Co up-hill diffusion behavior has to be elucidated yet, which is a subject of a separate study.

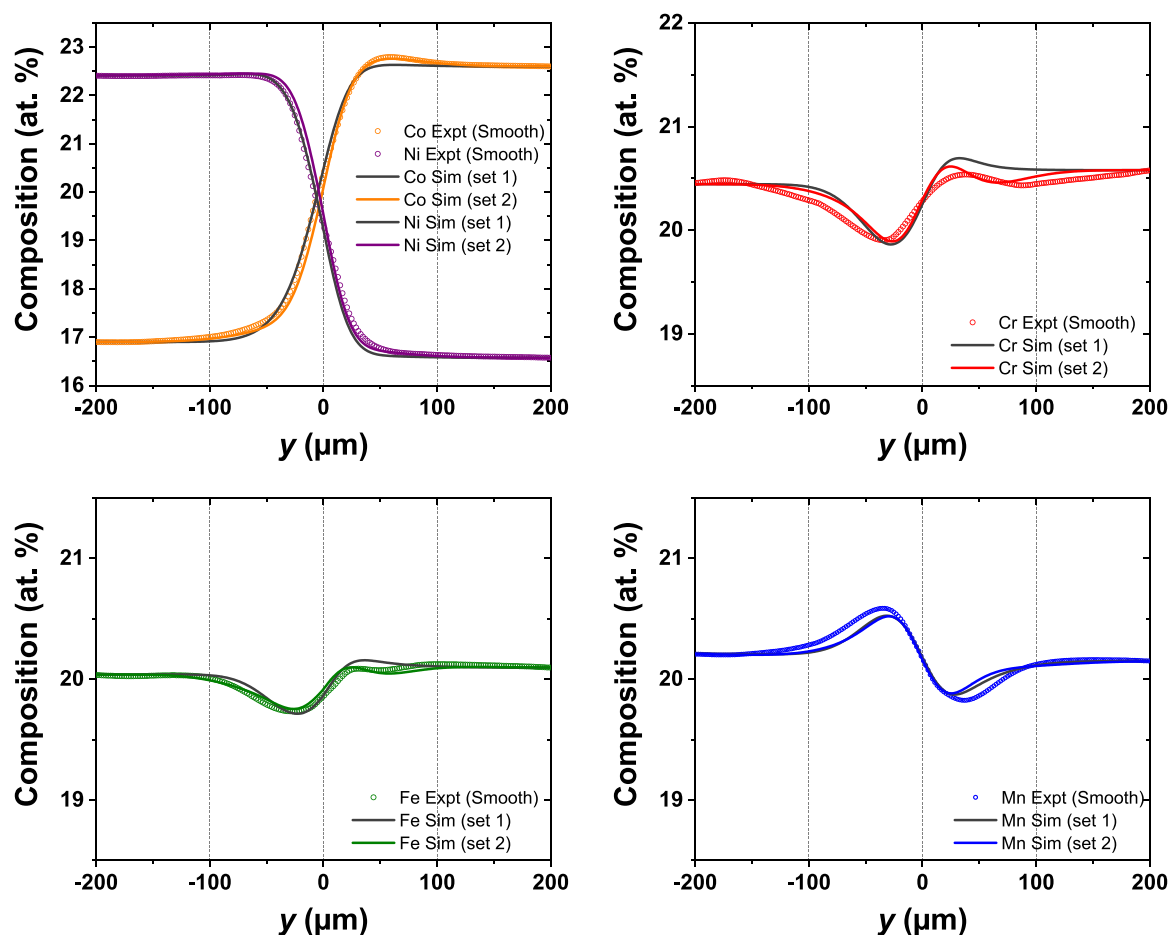


Figure 6. Comparison between the experimentally measured and smoothed with simulated interdiffusion profiles in Co-17/23 with increasing Co content near the Matano plane at 1373 K after 48 h for set 1 and set 2.

4. Summary

In the present work, the concentration-dependent tracer diffusion coefficients and the tracer diffusion coefficients of the unaffected end-members in a high-entropy Co-17/23 diffusion couple is determined under identical experimental conditions to the previously investigated Co-15/25 diffusion couple using the augmented tracer/interdiffusion approach. We found that the augmented tracer/interdiffusion couple approach can produce consistent diffusion databases in a high-throughput way. The obtained concentration-dependent tracer diffusion coefficients can be used to validate the existing multi-component diffusion databases.

- Tracer diffusion coefficients in the unaffected end-members of the diffusion couple are higher in the Ni-enriched alloys than in the Co-enriched alloys by about 50–70% for the slower elements like Co and Ni and up to 100% for the fast diffusing element (Mn).
- Comparing the two cases, i.e. Co-15/25 and Co-17/23 couples, the concentration-dependent tracer diffusion coefficients of the constituents in both diffusion couples are found to be generally in good agreement with each other and also in good agreement with the independently measured tracer diffusion coefficients in the unaffected end-members.
- Co shows opposite trends of the diffusion coefficients along the diffusion paths in the two couples, which is still within the experimental uncertainties. The deviations are largest for Cr.
- The estimation of the intrinsic and interdiffusion coefficients for the multicomponent diffusion couple following the augmented tracer/interdiffusion couple approach is demonstrated for the first time, highlighting the role of the vacancy wind effect.

CRediT authorship contribution statement

Daniel Gaertner: Writing - original draft, radiotracer experiments, and characterization. **Julia Kundin:** theoretical model derivation and simulations. **Neelamegan Esakkiraja:** Interdiffusion analysis, writing, review & editing. **Josua Kottke:** radiotracer experiments. **Jasper Bernt:** EPMA analysis. **Adeline Durand:** alloy processing and characterization. **Stephen Klemme:** review, supervision. **Guillaume Laplanche:** alloy processing, Writing review & editing. **Gunther Eggeler:** Writing review & editing, supervision. **Gerhard Wilde:** Writing review & editing, supervision. **Aloke Paul:** Interdiffusion analysis and supervision. **Ingo Steinbach:** theoretical derivation model and supervision. **Sergiy V. Divinski:** conceptualization, Writing review & editing and supervision.

Data availability

Data will be made available on request.

Declaration of Competing Interest

The authors declare that they have no known competing financial interests or personal relationships that could have appeared to influence the work reported in this paper.

Acknowledgement

Financial support from the Deutsche Forschungsgemeinschaft (DFG) via research projects DI 1419/13-2, STE 116/30-2 and LA3607/3/2 is acknowledged.

Appendix A. Appendix

Tables A1, A2, A3, A4, A5.
Figure A1.

Table A1

Thermodynamic factors (ϕ_{ij}^{Ni}), vacancy wind factors ($1 + W_{ij}^{Ni}$), intrinsic diffusion coefficients (D_{ij}^{Ni}) and interdiffusion coefficients (\bar{D}_{ij}^{Ni}) estimated at the composition A considering Ni as dependent component.

ϕ_{ij}^{Ni}		$1 + W_{ij}^{Ni}$		D_{ij}^{Ni}	($\times 10^{-15}$ m ² /s)	\bar{D}_{ij}^{Ni}	($\times 10^{-15}$ m ² /s)
ϕ_{CoCo}^{Ni}	1.0073	$1 + W_{CoCo}^{Ni}$	1.0204	D_{CoCo}^{Ni}	1.8430	\bar{D}_{CoCo}^{Ni}	1.4716
ϕ_{CoCr}^{Ni}	-0.4256	$1 + W_{CoCr}^{Ni}$	0.7542	D_{CoCr}^{Ni}	-0.5133	\bar{D}_{CoCr}^{Ni}	-2.1274
ϕ_{CoFe}^{Ni}	-0.2469	$1 + W_{CoFe}^{Ni}$	0.6787	D_{CoFe}^{Ni}	-0.2701	\bar{D}_{CoFe}^{Ni}	-1.5039
ϕ_{CoMn}^{Ni}	-0.4009	$1 + W_{CoMn}^{Ni}$	0.5063	D_{CoMn}^{Ni}	-0.3138	\bar{D}_{CoMn}^{Ni}	-3.2649
ϕ_{CrCo}^{Ni}	-0.2010	$1 + W_{CrCo}^{Ni}$	0.8975	D_{CrCo}^{Ni}	-0.7070	\bar{D}_{CrCo}^{Ni}	-1.1235
ϕ_{CrCr}^{Ni}	0.9677	$1 + W_{CrCr}^{Ni}$	1.1081	D_{CrCr}^{Ni}	4.2017	\bar{D}_{CrCr}^{Ni}	2.3921
ϕ_{CrFe}^{Ni}	-0.0687	$1 + W_{CrFe}^{Ni}$	-0.1544	D_{CrFe}^{Ni}	0.0419	\bar{D}_{CrFe}^{Ni}	-1.3413
ϕ_{CrMn}^{Ni}	0.2422	$1 + W_{CrMn}^{Ni}$	1.8169	D_{CrMn}^{Ni}	1.6668	\bar{D}_{CrMn}^{Ni}	-1.6417
ϕ_{FeCo}^{Ni}	-0.0521	$1 + W_{FeCo}^{Ni}$	0.6050	D_{FeCo}^{Ni}	-0.1260	\bar{D}_{FeCo}^{Ni}	-0.5391
ϕ_{FeCr}^{Ni}	-0.0790	$1 + W_{FeCr}^{Ni}$	-0.3237	D_{FeCr}^{Ni}	0.0911	\bar{D}_{FeCr}^{Ni}	-1.7040
ϕ_{FeFe}^{Ni}	1.0032	$1 + W_{FeFe}^{Ni}$	1.0791	D_{FeFe}^{Ni}	3.8878	\bar{D}_{FeFe}^{Ni}	2.5157
ϕ_{FeMn}^{Ni}	0.0193	$1 + W_{FeMn}^{Ni}$	11.2637	D_{FeMn}^{Ni}	0.7477	\bar{D}_{FeMn}^{Ni}	-2.5342
ϕ_{MnCo}^{Ni}	0.1948	$1 + W_{MnCo}^{Ni}$	1.1057	D_{MnCo}^{Ni}	2.1010	\bar{D}_{MnCo}^{Ni}	1.6702
ϕ_{MnCr}^{Ni}	0.6398	$1 + W_{MnCr}^{Ni}$	1.1635	D_{MnCr}^{Ni}	6.4773	\bar{D}_{MnCr}^{Ni}	4.6049
ϕ_{MnFe}^{Ni}	0.4306	$1 + W_{MnFe}^{Ni}$	1.1842	D_{MnFe}^{Ni}	4.4726	\bar{D}_{MnFe}^{Ni}	3.0414
ϕ_{MnMn}^{Ni}	1.7138	$1 + W_{MnMn}^{Ni}$	1.1155	D_{MnMn}^{Ni}	16.0771	\bar{D}_{MnMn}^{Ni}	12.6538
ϕ_{NiCo}^{Ni}	-0.7659	$1 + W_{NiCo}^{Ni}$	0.9731	D_{NiCo}^{Ni}	-1.0185	-	-
ϕ_{NiCr}^{Ni}	-1.0589	$1 + W_{NiCr}^{Ni}$	0.9012	D_{NiCr}^{Ni}	-1.1631	-	-
ϕ_{NiFe}^{Ni}	-1.0407	$1 + W_{NiFe}^{Ni}$	0.9238	D_{NiFe}^{Ni}	-1.1812	-	-
ϕ_{NiMn}^{Ni}	-1.5153	$1 + W_{NiMn}^{Ni}$	0.8694	D_{NiMn}^{Ni}	-1.5519	-	-

Table A2

Thermodynamic factors (ϕ_{ij}^{Ni}), vacancy wind factors ($1 + W_{ij}^{Ni}$), intrinsic diffusion coefficients (D_{ij}^{Ni}) and interdiffusion coefficients (\bar{D}_{ij}^{Ni}) estimated at the composition C considering Ni as dependent component.

ϕ_{ij}^{Ni}		$1 + W_{ij}^{Ni}$		D_{ij}^{Ni}	($\times 10^{-15}$ m ² /s)	\bar{D}_{ij}^{Ni}	($\times 10^{-15}$ m ² /s)
ϕ_{CoCo}^{Ni}	1.0115	$1 + W_{CoCo}^{Ni}$	1.0239	D_{CoCo}^{Ni}	1.6811	\bar{D}_{CoCo}^{Ni}	1.2707
ϕ_{CoCr}^{Ni}	-0.4152	$1 + W_{CoCr}^{Ni}$	0.7381	D_{CoCr}^{Ni}	-0.4761	\bar{D}_{CoCr}^{Ni}	-2.2214
ϕ_{CoFe}^{Ni}	-0.2439	$1 + W_{CoFe}^{Ni}$	0.6673	D_{CoFe}^{Ni}	-0.2571	\bar{D}_{CoFe}^{Ni}	-1.5815
ϕ_{CoMn}^{Ni}	-0.3976	$1 + W_{CoMn}^{Ni}$	0.4658	D_{CoMn}^{Ni}	-0.2833	\bar{D}_{CoMn}^{Ni}	-3.6388
ϕ_{CrCo}^{Ni}	-0.2090	$1 + W_{CrCo}^{Ni}$	0.8845	D_{CrCo}^{Ni}	-0.6483	\bar{D}_{CrCo}^{Ni}	-1.0771
ϕ_{CrCr}^{Ni}	0.9730	$1 + W_{CrCr}^{Ni}$	1.1118	D_{CrCr}^{Ni}	3.7931	\bar{D}_{CrCr}^{Ni}	1.9697
ϕ_{CrFe}^{Ni}	-0.0640	$1 + W_{CrFe}^{Ni}$	-0.2684	D_{CrFe}^{Ni}	0.0612	\bar{D}_{CrFe}^{Ni}	-1.3224
ϕ_{CrMn}^{Ni}	0.2344	$1 + W_{CrMn}^{Ni}$	1.9063	D_{CrMn}^{Ni}	1.5420	\bar{D}_{CrMn}^{Ni}	-1.9637
ϕ_{FeCo}^{Ni}	-0.0586	$1 + W_{FeCo}^{Ni}$	0.5884	D_{FeCo}^{Ni}	-0.1150	\bar{D}_{FeCo}^{Ni}	-0.5367
ϕ_{FeCr}^{Ni}	-0.0751	$1 + W_{FeCr}^{Ni}$	-0.4471	D_{FeCr}^{Ni}	0.1072	\bar{D}_{FeCr}^{Ni}	-1.6863
ϕ_{FeFe}^{Ni}	1.0017	$1 + W_{FeFe}^{Ni}$	1.0810	D_{FeFe}^{Ni}	3.5116	\bar{D}_{FeFe}^{Ni}	2.1507
ϕ_{FeMn}^{Ni}	0.0165	$1 + W_{FeMn}^{Ni}$	13.8685	D_{FeMn}^{Ni}	0.7186	\bar{D}_{FeMn}^{Ni}	-2.7294
ϕ_{MnCo}^{Ni}	0.2073	$1 + W_{MnCo}^{Ni}$	1.1164	D_{MnCo}^{Ni}	2.1643	\bar{D}_{MnCo}^{Ni}	1.7287
ϕ_{MnCr}^{Ni}	0.6419	$1 + W_{MnCr}^{Ni}$	1.1694	D_{MnCr}^{Ni}	6.7181	\bar{D}_{MnCr}^{Ni}	4.8657
ϕ_{MnFe}^{Ni}	0.4303	$1 + W_{MnFe}^{Ni}$	1.1886	D_{MnFe}^{Ni}	4.6544	\bar{D}_{MnFe}^{Ni}	3.2488
ϕ_{MnMn}^{Ni}	1.7017	$1 + W_{MnMn}^{Ni}$	1.1248	D_{MnMn}^{Ni}	16.8630	\bar{D}_{MnMn}^{Ni}	13.3016
ϕ_{NiCo}^{Ni}	-0.8932	$1 + W_{NiCo}^{Ni}$	0.9730	D_{NiCo}^{Ni}	-0.9480	-	-
ϕ_{NiCr}^{Ni}	-1.1299	$1 + W_{NiCr}^{Ni}$	0.9038	D_{NiCr}^{Ni}	-1.0662	-	-
ϕ_{NiFe}^{Ni}	-1.1015	$1 + W_{NiFe}^{Ni}$	0.9263	D_{NiFe}^{Ni}	-1.0831	-	-
ϕ_{NiMn}^{Ni}	-1.5657	$1 + W_{NiMn}^{Ni}$	0.8643	D_{NiMn}^{Ni}	-1.3908	-	-

Table A3

Thermodynamic factors (ϕ_{ij}^{Ni}), vacancy wind factors ($1 + W_{ij}^{Ni}$), intrinsic diffusion coefficients (D_{ij}^{Ni}) and interdiffusion coefficients (\tilde{D}_{ij}^{Ni}) estimated at the composition D considering Ni as dependent component.

ϕ_{ij}^{Ni}		$1 + W_{ij}^{Ni}$		D_{ij}^{Ni}	($\times 10^{-15}$ m ² /s)	\tilde{D}_{ij}^{Ni}	($\times 10^{-15}$ m ² /s)
ϕ_{CoCo}^{Ni}	1.0146	$1 + W_{CoCo}^{Ni}$	1.0258	D_{CoCo}^{Ni}	1.6993	\tilde{D}_{CoCo}^{Ni}	1.2568
ϕ_{CoCr}^{Ni}	-0.4088	$1 + W_{CoCr}^{Ni}$	0.7295	D_{CoCr}^{Ni}	-0.4844	\tilde{D}_{CoCr}^{Ni}	-2.3451
ϕ_{CoFe}^{Ni}	-0.2424	$1 + W_{CoFe}^{Ni}$	0.6688	D_{CoFe}^{Ni}	-0.2688	\tilde{D}_{CoFe}^{Ni}	-1.6476
ϕ_{CoMn}^{Ni}	-0.3938	$1 + W_{CoMn}^{Ni}$	0.4529	D_{CoMn}^{Ni}	-0.2899	\tilde{D}_{CoMn}^{Ni}	-3.9173
ϕ_{CrCo}^{Ni}	-0.2128	$1 + W_{CrCo}^{Ni}$	0.8772	D_{CrCo}^{Ni}	-0.6487	\tilde{D}_{CrCo}^{Ni}	-1.0934
ϕ_{CrCr}^{Ni}	0.9768	$1 + W_{CrCr}^{Ni}$	1.1132	D_{CrCr}^{Ni}	3.7783	\tilde{D}_{CrCr}^{Ni}	1.9084
ϕ_{CrFe}^{Ni}	-0.0608	$1 + W_{CrFe}^{Ni}$	-0.3211	D_{CrFe}^{Ni}	0.0692	\tilde{D}_{CrFe}^{Ni}	-1.3164
ϕ_{CrMn}^{Ni}	0.2291	$1 + W_{CrMn}^{Ni}$	1.9407	D_{CrMn}^{Ni}	1.5454	\tilde{D}_{CrMn}^{Ni}	-2.1000
ϕ_{FeCo}^{Ni}	-0.0628	$1 + W_{FeCo}^{Ni}$	0.5837	D_{FeCo}^{Ni}	-0.1120	\tilde{D}_{FeCo}^{Ni}	-0.5477
ϕ_{FeCr}^{Ni}	-0.0726	$1 + W_{FeCr}^{Ni}$	-0.5233	D_{FeCr}^{Ni}	0.1056	\tilde{D}_{FeCr}^{Ni}	-1.7164
ϕ_{FeFe}^{Ni}	1.0005	$1 + W_{FeFe}^{Ni}$	1.0802	D_{FeFe}^{Ni}	3.3555	\tilde{D}_{FeFe}^{Ni}	1.9979
ϕ_{FeMn}^{Ni}	0.0149	$1 + W_{FeMn}^{Ni}$	15.4565	D_{FeMn}^{Ni}	0.7012	\tilde{D}_{FeMn}^{Ni}	-2.8704
ϕ_{MnCo}^{Ni}	0.2148	$1 + W_{MnCo}^{Ni}$	1.1216	D_{MnCo}^{Ni}	2.2105	\tilde{D}_{MnCo}^{Ni}	1.7660
ϕ_{MnCr}^{Ni}	0.6442	$1 + W_{MnCr}^{Ni}$	1.1717	D_{MnCr}^{Ni}	6.8906	\tilde{D}_{MnCr}^{Ni}	5.0217
ϕ_{MnFe}^{Ni}	0.4316	$1 + W_{MnFe}^{Ni}$	1.1860	D_{MnFe}^{Ni}	4.7696	\tilde{D}_{MnFe}^{Ni}	3.3846
ϕ_{MnMn}^{Ni}	1.6921	$1 + W_{MnMn}^{Ni}$	1.1274	D_{MnMn}^{Ni}	17.4228	\tilde{D}_{MnMn}^{Ni}	13.7792
ϕ_{NiCo}^{Ni}	-0.9827	$1 + W_{NiCo}^{Ni}$	0.9734	D_{NiCo}^{Ni}	-0.9521	–	–
ϕ_{NiCr}^{Ni}	-1.1824	$1 + W_{NiCr}^{Ni}$	0.9065	D_{NiCr}^{Ni}	-1.0616	–	–
ϕ_{NiFe}^{Ni}	-1.1481	$1 + W_{NiFe}^{Ni}$	0.9301	D_{NiFe}^{Ni}	-1.0795	–	–
ϕ_{NiMn}^{Ni}	-1.5966	$1 + W_{NiMn}^{Ni}$	0.8650	D_{NiMn}^{Ni}	-1.3687	–	–

Table A4

Thermodynamic factors (ϕ_{ij}^{Ni}), vacancy wind factors ($1 + W_{ij}^{Ni}$), intrinsic diffusion coefficients (D_{ij}^{Ni}) and interdiffusion coefficients (\tilde{D}_{ij}^{Ni}) estimated at the composition E considering Ni as dependent component.

ϕ_{ij}^{Ni}		$1 + W_{ij}^{Ni}$		D_{ij}^{Ni}	($\times 10^{-15}$ m ² /s)	\tilde{D}_{ij}^{Ni}	($\times 10^{-15}$ m ² /s)
ϕ_{CoCo}^{Ni}	1.0172	$1 + W_{CoCo}^{Ni}$	1.0225	D_{CoCo}^{Ni}	1.5097	\tilde{D}_{CoCo}^{Ni}	1.1514
ϕ_{CoCr}^{Ni}	-0.4030	$1 + W_{CoCr}^{Ni}$	0.7234	D_{CoCr}^{Ni}	-0.4344	\tilde{D}_{CoCr}^{Ni}	-2.2405
ϕ_{CoFe}^{Ni}	-0.2412	$1 + W_{CoFe}^{Ni}$	0.6854	D_{CoFe}^{Ni}	-0.2518	\tilde{D}_{CoFe}^{Ni}	-1.5094
ϕ_{CoMn}^{Ni}	-0.3895	$1 + W_{CoMn}^{Ni}$	0.4644	D_{CoMn}^{Ni}	-0.2739	\tilde{D}_{CoMn}^{Ni}	-3.7100
ϕ_{CrCo}^{Ni}	-0.2153	$1 + W_{CrCo}^{Ni}$	0.8936	D_{CrCo}^{Ni}	-0.6621	\tilde{D}_{CrCo}^{Ni}	-1.0111
ϕ_{CrCr}^{Ni}	0.9803	$1 + W_{CrCr}^{Ni}$	1.1137	D_{CrCr}^{Ni}	3.7570	\tilde{D}_{CrCr}^{Ni}	1.9975
ϕ_{CrFe}^{Ni}	-0.0577	$1 + W_{CrFe}^{Ni}$	-0.3162	D_{CrFe}^{Ni}	0.0642	\tilde{D}_{CrFe}^{Ni}	-1.1609
ϕ_{CrMn}^{Ni}	0.2248	$1 + W_{CrMn}^{Ni}$	1.9280	D_{CrMn}^{Ni}	1.5159	\tilde{D}_{CrMn}^{Ni}	-1.8316
ϕ_{FeCo}^{Ni}	-0.0663	$1 + W_{FeCo}^{Ni}$	0.6543	D_{FeCo}^{Ni}	-0.1150	\tilde{D}_{FeCo}^{Ni}	-0.4565
ϕ_{FeCr}^{Ni}	-0.0702	$1 + W_{FeCr}^{Ni}$	-0.5887	D_{FeCr}^{Ni}	0.1123	\tilde{D}_{FeCr}^{Ni}	-1.6089
ϕ_{FeFe}^{Ni}	0.9998	$1 + W_{FeFe}^{Ni}$	1.0759	D_{FeFe}^{Ni}	2.9913	\tilde{D}_{FeFe}^{Ni}	1.7929
ϕ_{FeMn}^{Ni}	0.0139	$1 + W_{FeMn}^{Ni}$	16.0521	D_{FeMn}^{Ni}	0.6151	\tilde{D}_{FeMn}^{Ni}	-2.6594
ϕ_{MnCo}^{Ni}	0.2210	$1 + W_{MnCo}^{Ni}$	1.1037	D_{MnCo}^{Ni}	1.9755	\tilde{D}_{MnCo}^{Ni}	1.6321
ϕ_{MnCr}^{Ni}	0.6465	$1 + W_{MnCr}^{Ni}$	1.1724	D_{MnCr}^{Ni}	6.3004	\tilde{D}_{MnCr}^{Ni}	4.5694
ϕ_{MnFe}^{Ni}	0.4336	$1 + W_{MnFe}^{Ni}$	1.1750	D_{MnFe}^{Ni}	4.3298	\tilde{D}_{MnFe}^{Ni}	3.1246
ϕ_{MnMn}^{Ni}	1.6833	$1 + W_{MnMn}^{Ni}$	1.1239	D_{MnMn}^{Ni}	15.9860	\tilde{D}_{MnMn}^{Ni}	12.6927
ϕ_{NiCo}^{Ni}	-1.0649	$1 + W_{NiCo}^{Ni}$	0.9785	D_{NiCo}^{Ni}	-0.9942	–	–
ϕ_{NiCr}^{Ni}	-1.2307	$1 + W_{NiCr}^{Ni}$	0.9094	D_{NiCr}^{Ni}	-1.0962	–	–
ϕ_{NiFe}^{Ni}	-1.1929	$1 + W_{NiFe}^{Ni}$	0.9364	D_{NiFe}^{Ni}	-1.1184	–	–
ϕ_{NiMn}^{Ni}	-1.6219	$1 + W_{NiMn}^{Ni}$	0.8714	D_{NiMn}^{Ni}	-1.4071	–	–

Table A5

Thermodynamic factors (ϕ_{ij}^{Ni}), vacancy wind factors ($1 + W_{ij}^{Ni}$), intrinsic diffusion coefficients (D_{ij}^{Ni}) and interdiffusion coefficients (\tilde{D}_{ij}^{Ni}) estimated at the composition F considering Ni as dependent component.

ϕ_{ij}^{Ni}		$1 + W_{ij}^{Ni}$		D_{ij}^{Ni}	($\times 10^{-15} \text{ m}^2/\text{s}$)	\tilde{D}_{ij}^{Ni}	($\times 10^{-15} \text{ m}^2/\text{s}$)
ϕ_{CoCo}^{Ni}	1.0197	$1 + W_{CoCo}^{Ni}$	1.0204	D_{CoCo}^{Ni}	1.4779	\tilde{D}_{CoCo}^{Ni}	1.1908
ϕ_{CoCr}^{Ni}	-0.3968	$1 + W_{CoCr}^{Ni}$	0.7230	D_{CoCr}^{Ni}	-0.4320	\tilde{D}_{CoCr}^{Ni}	-2.0851
ϕ_{CoFe}^{Ni}	-0.2405	$1 + W_{CoFe}^{Ni}$	0.7148	D_{CoFe}^{Ni}	-0.2645	\tilde{D}_{CoFe}^{Ni}	-1.3186
ϕ_{CoMn}^{Ni}	-0.3870	$1 + W_{CoMn}^{Ni}$	0.5114	D_{CoMn}^{Ni}	-0.3062	\tilde{D}_{CoMn}^{Ni}	-3.2282
ϕ_{CrCo}^{Ni}	-0.2179	$1 + W_{CrCo}^{Ni}$	0.9044	D_{CrCo}^{Ni}	-0.6864	\tilde{D}_{CrCo}^{Ni}	-0.9572
ϕ_{CrCr}^{Ni}	0.9831	$1 + W_{CrCr}^{Ni}$	1.1118	D_{CrCr}^{Ni}	3.8063	\tilde{D}_{CrCr}^{Ni}	2.2470
ϕ_{CrFe}^{Ni}	-0.0553	$1 + W_{CrFe}^{Ni}$	-0.2413	D_{CrFe}^{Ni}	0.0474	\tilde{D}_{CrFe}^{Ni}	-0.9468
ϕ_{CrMn}^{Ni}	0.2201	$1 + W_{CrMn}^{Ni}$	1.8589	D_{CrMn}^{Ni}	1.4645	\tilde{D}_{CrMn}^{Ni}	-1.2917
ϕ_{FeCo}^{Ni}	-0.0703	$1 + W_{FeCo}^{Ni}$	0.7035	D_{FeCo}^{Ni}	-0.1118	\tilde{D}_{FeCo}^{Ni}	-0.3769
ϕ_{FeCr}^{Ni}	-0.0682	$1 + W_{FeCr}^{Ni}$	-0.6112	D_{FeCr}^{Ni}	0.1000	\tilde{D}_{FeCr}^{Ni}	-1.4260
ϕ_{FeFe}^{Ni}	0.9987	$1 + W_{FeFe}^{Ni}$	1.0687	D_{FeFe}^{Ni}	2.6146	\tilde{D}_{FeFe}^{Ni}	1.6416
ϕ_{FeMn}^{Ni}	0.0124	$1 + W_{FeMn}^{Ni}$	16.2653	D_{FeMn}^{Ni}	0.4964	\tilde{D}_{FeMn}^{Ni}	-2.2009
ϕ_{MnCo}^{Ni}	0.2271	$1 + W_{MnCo}^{Ni}$	1.0918	D_{MnCo}^{Ni}	1.6065	\tilde{D}_{MnCo}^{Ni}	1.3430
ϕ_{MnCr}^{Ni}	0.6469	$1 + W_{MnCr}^{Ni}$	1.1699	D_{MnCr}^{Ni}	5.1993	\tilde{D}_{MnCr}^{Ni}	3.6821
ϕ_{MnFe}^{Ni}	0.4356	$1 + W_{MnFe}^{Ni}$	1.1575	D_{MnFe}^{Ni}	3.5396	\tilde{D}_{MnFe}^{Ni}	2.5722
ϕ_{MnMn}^{Ni}	1.6761	$1 + W_{MnMn}^{Ni}$	1.1128	D_{MnMn}^{Ni}	13.1694	\tilde{D}_{MnMn}^{Ni}	10.4876
ϕ_{NiCo}^{Ni}	-1.1600	$1 + W_{NiCo}^{Ni}$	0.9820	D_{NiCo}^{Ni}	-0.9626	-	-
ϕ_{NiCr}^{Ni}	-1.2854	$1 + W_{NiCr}^{Ni}$	0.9145	D_{NiCr}^{Ni}	-1.0531	-	-
ϕ_{NiFe}^{Ni}	-1.2465	$1 + W_{NiFe}^{Ni}$	0.9449	D_{NiFe}^{Ni}	-1.0783	-	-
ϕ_{NiMn}^{Ni}	-1.6600	$1 + W_{NiMn}^{Ni}$	0.8861	D_{NiMn}^{Ni}	-1.3543	-	-

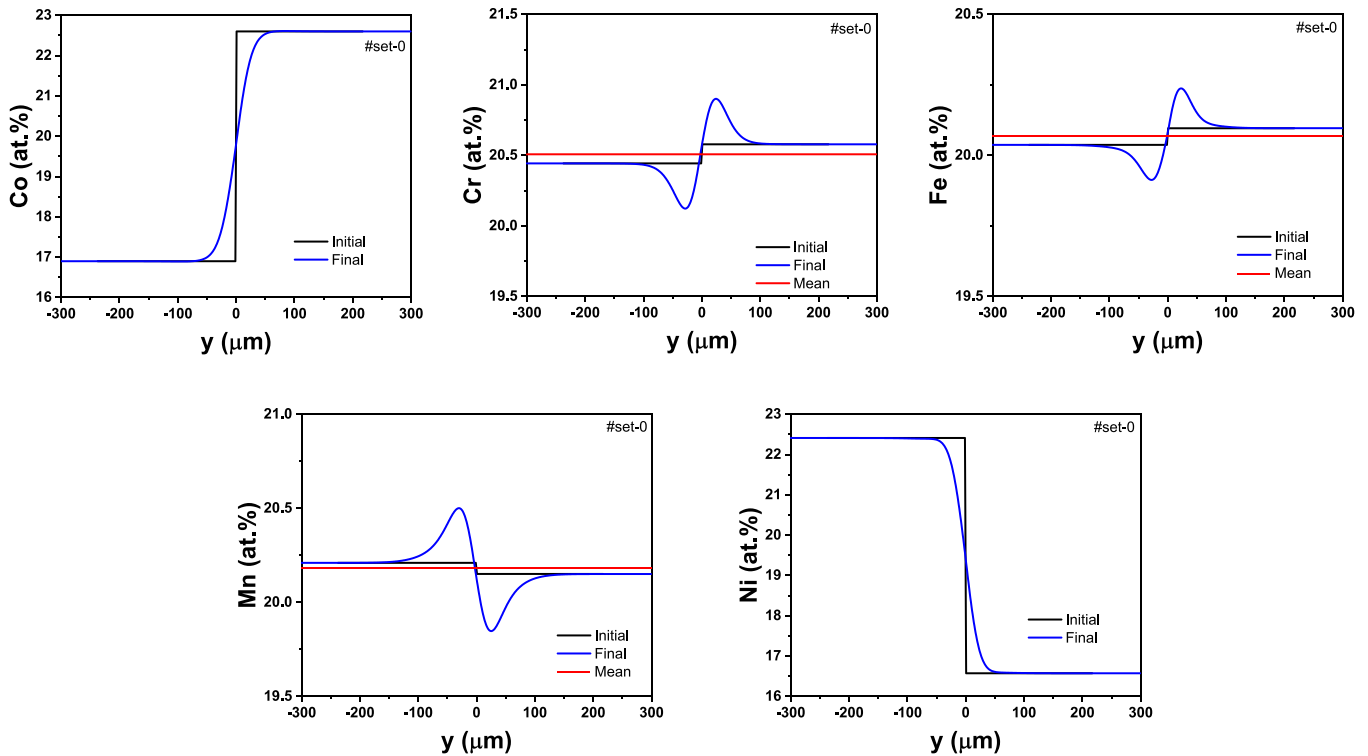


Fig. A1. Comparison of model initial (black lines) and final (blue lines) interdiffusion profiles for ideal diffusion couple (with homogeneous end-members). The red lines correspond to averaged compositions and visualize differences in end-member compositions for the elements with nominal concentration about 20%.

References

- [1] D.B. Miracle, O.N. Senkov, A critical review of high entropy alloys and related concepts, *Acta Mater.* 122 (2017) 448–511.
- [2] S.V. Divinski, A. Pokoev, N. Esakkiraja, A. Paul, A mystery of 'sluggish diffusion' in High-Entropy Alloys: the Truth or a Myth? *Diffus. Found.* 17 (2018) 69–104.
- [3] S.V. Divinski, O.A. Lukianova, A. Dash, N. Esakkiraja, G. Wilde, A. Paul, High-entropy alloys: diffusion, *Encycl. Mater. Met. Alloy.* 2 (2022) 402–416.
- [4] J. Daabrowa, M. Danielewski, State-of-the-Art diffusion studies in the high entropy alloys, *Metals* 10 (3) (2020) 347.
- [5] B. Cantor, Multicomponent and high entropy alloys, *Entropy* 16 (9) (2014) 4749–4768.
- [6] D.L. Beke, G. Erdélyi, On the diffusion in high-entropy alloys, *Mater. Lett.* 164 (2016) 111–113 (feb).
- [7] T.R. Paul, I.V. Belova, G.E. Murch, Random alloy diffusion kinetics for the application to multicomponent alloy systems, *Philos. Mag.* 96 (12) (2016) 1228–1244.
- [8] W. Kucza, J. Daabrowa, G. Cieślak, K. Berent, T. Kulik, M. Danielewski, Studies of "sluggish diffusion" effect in Co-Cr-Fe-Mn-Ni, Co-Cr-Fe-Ni and Co-Fe-Mn-Ni high entropy alloys; determination of tracer diffusivities by combinatorial approach, *J. Alloy. Compd.* 731 (2018) 920–928.
- [9] W. Chen, L. Zhang, High-throughput determination of interdiffusion coefficients for Co-Cr-Fe-Mn-Ni high-entropy alloys, *J. Phase Equilibria Diffus.* 38 (2017) 457–465.
- [10] K.Y. Tsai, M.H. Tsai, J.W. Yeh, Sluggish diffusion in Co-Cr-Fe-Mn-Ni high-entropy alloys, *Acta Mater.* 61 (2013) 4887–4897.
- [11] A. Durand, L. Peng, G. Laplanche, J.R. Morris, E.P. George, G. Eggeler, Interdiffusion in Cr-Fe-Co-Ni medium-entropy alloys, *Intermetallics* 122 (2020) 106789.
- [12] M. Vaidya, S. Trubel, B.S. Murty, G. Wilde, S.V. Divinski, Ni tracer diffusion in CoCrFeNi and CoCrFeMnNi high entropy alloys, *J. Alloy. Compd.* 688 (2016) 994–1001.
- [13] M. Vaidya, K.G. Pradeep, B.S. Murty, G. Wilde, S.V. Divinski, Bulk tracer diffusion in CoCrFeNi and CoCrFeMnNi high entropy alloys, *Acta Mater.* 146 (2018) 211–224 (mar).
- [14] D. Gaertner, J. Kottke, G. Wilde, S.V. Divinski, Y. Chumlyakov, Tracer diffusion in single crystalline CoCrFeNi and CoCrFeMnNi high entropy alloys, *J. Mater. Res.* 33 (19) (2018) 3184–3191.
- [15] D. Gaertner, J. Kottke, Y. Chumlyakov, F. Hergemöller, G. Wilde, S.V. Divinski, Tracer diffusion in single crystalline CoCrFeNi and CoCrFeMnNi high-entropy alloys: kinetic hints towards a low-temperature phase instability of the solid-solution? *Scr. Mater.* 187 (2020) 57–62.
- [16] I.V. Belova, N.S. Kulkarni, Y.H. Sohn, G.E. Murch, Simultaneous tracer diffusion and interdiffusion in a sandwich-type configuration to provide the composition dependence of the tracer diffusion coefficients, *Philos. Mag.* 94 (31) (2014) 3560–3573.
- [17] I.V. Belova, Y.H. Sohn, G.E. Murch, Measurement of tracer diffusion coefficients in an interdiffusion context for multicomponent alloys, *Philos. Mag. Lett.* 95 (8) (2015) 416–424.
- [18] J.R. Manning, Tracer diffusion in a chemical concentration gradient in silver-cadmium, *Phys. Rev.* 116 (1) (1959) 69–79.
- [19] D. Gaertner, K. Abrahams, J. Kottke, V.A. Esin, I. Steinbach, G. Wilde, S.V. Divinski, Concentration-dependent atomic mobilities in FCC CoCrFeMnNi high-entropy alloys, *Acta Mater.* 166 (2019) 357–370.
- [20] Thermo-Calc Software. TCFE Steels/Fe-alloys Database Version 9, 2017.
- [21] Thermo-Calc Software. TCNI Ni-based Superalloys Database Version 8, 2018.
- [22] J.R. Manning, Cross terms in the thermodynamic diffusion equations for multicomponent alloys, *Metall. Mater. Trans.* 1 (1970) 499–505.
- [23] N. Esakkiraja, A. Dash, A. Mondal, K.C. HariKumar, A. Paul, Correlation between estimated diffusion coefficients from different types of diffusion couples in multicomponent system, *Materialia* 16 (2021) 101046.
- [24] J. Kundin, I. Steinbach, K. Abrahams, S.V. Divinski, Pair-exchange diffusion model for multicomponent alloys revisited, *Materialia* 16 (2021) 101047.
- [25] M. Schneider, F. Werner, D. Langenkämper, Ch. Reinhart, G. Laplanche, Effect of temperature and texture on Hall-Petch strengthening by grain and annealing twin boundaries in the MnFeNi medium-entropy alloy, *Metals* 9 (2019) 84.
- [26] M. Schneider, E.P. George, T.J. Manescau, T. Zalezak, J. Hunfeld, A. Dlouhy, G. Eggeler, G. Laplanche, Analysis of strengthening due to grain boundaries and annealing twin boundaries in the CrCoNi medium-entropy alloy, *Int. J. Plast.* 124 (2020) 155–169.
- [27] Hans Lukas, Suzana G. Fries, Bo Sundman, *Computational Thermodynamics: The Calphad Method*, first ed, Cambridge University Press, New York, NY, USA, 2007.
- [28] C. Haase, F. Tang, M.B. Wilms, A. Weisheit, B. Hallstedt, Combining thermodynamic modeling and 3D printing of elemental powder blends for high-throughput investigation of high-entropy alloys - towards rapid alloy screening and design, *Mater. Sci. Eng. A* 688 (2017) 180–189.
- [29] A. Borgenstam, L. Höglund, J. Ågren, A. Engström, DICTRA, a tool for simulation of diffusional transformations in alloys, *J. Phase Equilibria* 21 (3) (2000) 269.
- [30] J.O. Andersson, J. Ågren, Models for numerical treatment of multicomponent diffusion in simple phases, *J. Appl. Phys.* 72 (1992) 1350–1355.
- [31] B. Jönsson, Ferromagnetic ordering and diffusion of carbon and nitrogen in bcc Cr-Fe-Ni alloys, *Z. Met.* 85 (1994) 498.
- [32] C.E. Campbell, A new technique for evaluating diffusion mobility parameters, *J. Phase Equilibria Diffus.* 26 (5) (2005) 435–440.
- [33] C.E. Campbell, Assessment of the diffusion mobilities in the γ' and B2 phases in the Ni-Al-Cr system, *Acta Mater.* 56 (16) (2008) 4277–4290.
- [34] O. Redlich, A. Kister, Algebraic representation of thermodynamic properties and the classification of solutions, *Ind. Eng. Chem.* 40 (1948) 345–348.
- [35] A. Paul, T. Laurila, V. Vuorinen, S.V. Divinski, *Thermodynamics, Diffusion and the Kirkendall Effect in Solids*, Springer International Publishing, 2014.
- [36] L. Onsager, Reciprocal relations in irreversible processes. I, *Phys. Rev.* 37 (1931) 405–426.
- [37] J.E. Lane, J.S. Kirkaldy, Diffusion in multicomponent metallic systems: VIII. A kinetic calculation of the Onsager L coefficients in substitutional solid solutions, *Can. J. Phys.* 42 (8) (1964) 1643–1657.
- [38] N. Esakkiraja, A. Dash, A. Mondal, K.C. HariKumar, A. Paul, Diffusion coefficients in multicomponent systems: an analysis based on a four-component system. HAL Archive (<https://hal.archives-ouvertes.fr/hal-03199589>), 2021.
- [39] H. Mehrer, *Diffusion in Solids*, Springer International Publishing, 2007.
- [40] J. Crank, *The Mathematics of Diffusion*, Oxford University Press, 1975.
- [41] F. Sauer, V. Freise, Diffusion in binären Gemischen mit Volumenänderung, *Z. Elektrochem.* 66 (4) (1962) 353–362.
- [42] Yu.E. Ugaste, A.A. Kodentsov, J. Priimets, Investigation of interdiffusion and kirkendall effect in the Co-Ni-Fe system: III. Dependence of diffusion parameters on the initial conditions, *Phys. Met. Metallogr.* 110 (2010) 485–491.
- [43] H. Leszczynski, K. Lademan, K.T. Smiech, B. Bozek, M. Zajusz, M. Danielewski, On the Matano plane position in multicomponent diffusion couples, *Nano Hybrid Compos.* 26 (2019) 20–29.